Chapter 9

DETECTOR BACKGROUND AND DETECTOR DESIGN

Contents

9.1 Introduction

In this chapter issues relating to the conceptual design of a detector for a 2 TeV $\times$ 2 TeV Muon Collider are discussed. The physics justification for a lepton collider in such an energy range has been extensively studied [1] ,[2]. Here design considerations specific to a muon

collider are considered. From the experimental point of view there are advantages and new challenges that must be faced in the design of the detector and the experimental area.

The detector is designed for a muon collider with $\sqrt{s} = 4$ TeV, an average luminosity of 10^{35} cm^{-2}s^{-1} and an integrated luminosity of 1000 fb^{-1}; beam crossings occur every 10 μs and each muon bunch has 2×10^{12} muons.

The physics benchmark used in determining the criteria for the detector was strong WW scattering resulting in W pairs, Z pairs and top quark pairs. The generic question of tagging b-decays in this environment is also being investigated. The list of physics topics being addressed will be expanded as the design matures but these two topics are potentially significant for this energy regime and provide significant constraints on the detector requirements.

A major advantage of a muon collider is the ability to recirculate the muons without an overwhelming radiative energy loss. The present assessment is that the muons will survive for about 1000 turns before the losses, primarily from muon decays, significantly reduce the luminosity. From a purely experimental point of view there are two notable advantages of muon colliders compared to electron colliders: the center of mass energy of the collisions is better defined, and at high energy the background process arising from double photon interactions is suppressed.

The experimental environment of a muon collider offers a new design challenge as the level of background, arising mostly from the interactions of electrons originating from muon decay to $e\nu_\mu\nu_e$, needs to be better understood and controlled.

In section 9.2 physics processes are discussed and the quantities that need to be measured outlined. In Section 9.3, the particular machine related background problems associated with muon colliders and the present conceptual design of an intersection region are discussed. In Section 9.4 the detector specifications and the conceptual design of a detector are presented. Some very preliminary results on machine backgrounds for a lower energy collider (250 GeV x 250 GeV) are presented in Section 9.5 while in Section 9.6 the present status of the current effort is summarized.

9.2 Physics Aspects of a 4 TeV $\mu^+\mu^-$ Collider

The physics goals of a $\mu^+\mu^-$ collider are discussed in Chapter 2. The larger muon mass does provide some possible advantages:

- s-channel Higgs production is enhanced by a factor of $(m_\mu/m_e)^2 \approx 40000$.
- QED radiation is reduced by a factor of $[\ln(\sqrt{s}/m_\mu)/\ln(\sqrt{s}/m_e)]^2$, leading to smaller $\gamma\gamma$ backgrounds and a smaller beam energy spread.

There are also disadvantages:

- Muon decays give large backgrounds and hence a more difficult environment for the experiments. These problems can be mitigated by careful shielding design.

The physics capabilities of $\mu^+\mu^-$ and e^+e^- colliders with the same energy and luminosity are similar, so that the choice between them will depend mainly on the feasibility and cost of the accelerators.

Possible strongly interacting W_LW_L cross sections from Barger[4] are shown in Fig. 2.13. For the present study a 1 TeV Higgs boson has been used. The signals and backgrounds were calculated using PYTHIA. The studies so far have used a toy detector and have not included machine related backgrounds. As these backgrounds are better understood, they will be included.

Fig. 9.1 shows the mass distribution for the 1 TeV Higgs signals and physics backgrounds from PYTHIA in a toy detector, which includes segmentation of $\Delta\eta = \Delta\phi = 0.05$ and the angular coverage, $20^\circ < \theta < 160^\circ$, assumed in the machine background calculations. Since the nominal luminosity is $1000\,\mathrm{fb}^{-1}$, there are $\gtrsim 1000$ events per bin at the peak. The loss in signal from the 20° cone is larger for this process than for s-channel processes but is still fairly small, as can be seen in Fig. 9.2. The dead cone has a larger effect on $\gamma\gamma \to WW$ and thus the accepted region has a better signal to background ratio.

It would be desirable to separate the WW and ZZ final states in purely hadronic modes by reconstructing the masses. Whether this is possible or not will depend on the details of the calorimeter performance and the level of the machine backgrounds. If it is not, then one can use the $\sim 12\%$ of events in which one $Z \to ee$ or $\mu\mu$ to determine the Z rate. Clearly there is a real challenge to try to measure the hadronic modes.

The background from $\gamma\gamma$ and γZ processes is smaller at a muon collider than at an electron collider but not negligible. Since the p_T of the photons is usually very small while the WW fusion process typically gives a p_T of order M_W, these backgrounds can be reduced by making a cut $p_{T,WW} > 50\,\mathrm{GeV}$, as shown in Fig. 9.3. This cut keeps most of the signal while significantly reducing the physics background. The present calculation is undoubtedly optimistic, since it neglects the degradation in resolution from the machine background, but an effective cut with an acceptable signal loss should be possible.

Tagging the outgoing muons would give an additional handle on separating $WW \to WW$ from $\gamma\gamma \to WW$, $\gamma Z \to WZ$, etc. Even after the $p_T > 50\,\mathrm{GeV}$ cut is made on the final state, most of these muons will be inside the 20° cone, as can be seen in Fig. 9.4. Tagging the muons inside the detector will be difficult. However, the muons will have $\gtrsim 1\,\mathrm{TeV}$, so

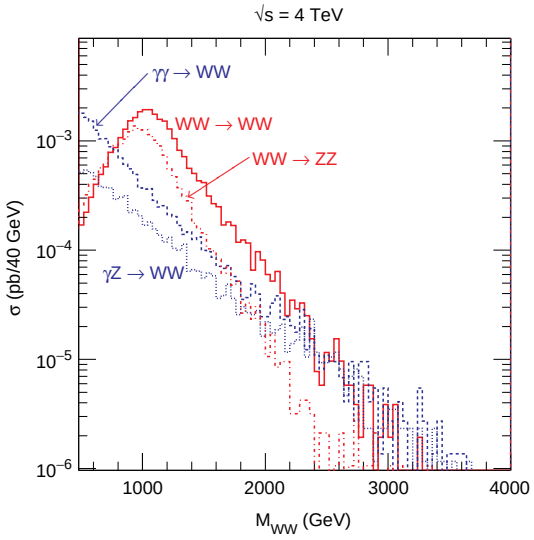

Figure 9.1: Signals and physics backgrounds for a 1 TeV Higgs boson at a $\mu\mu$ collider, including the effect of a 20° dead cone around the beamline.

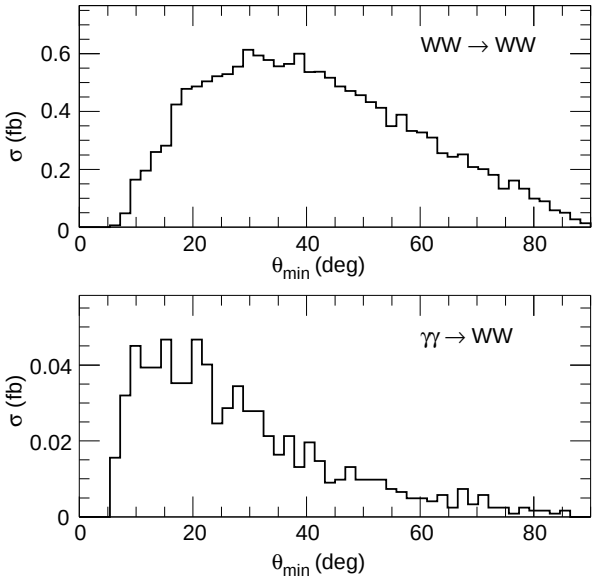

Figure 9.2: $WW \to WW$ signal and $\gamma\gamma \to WW$ background vs. the minimum angle, $\theta_{\min}$, of the W.

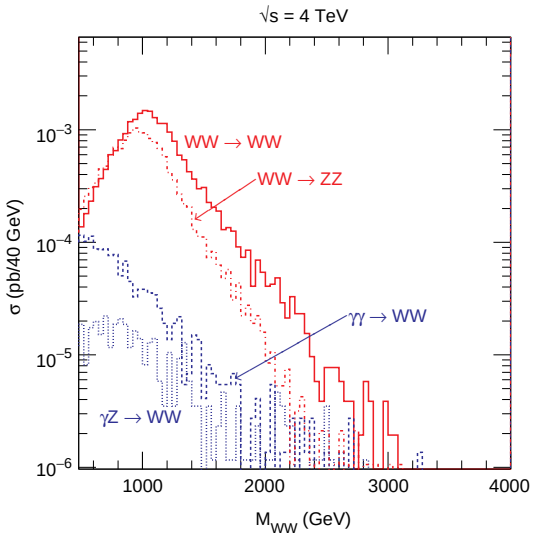

Figure 9.3: Signals and physics backgrounds for a 1 TeV Higgs boson with a cut $p_{T,WW} > 50\,\text{GeV}$.

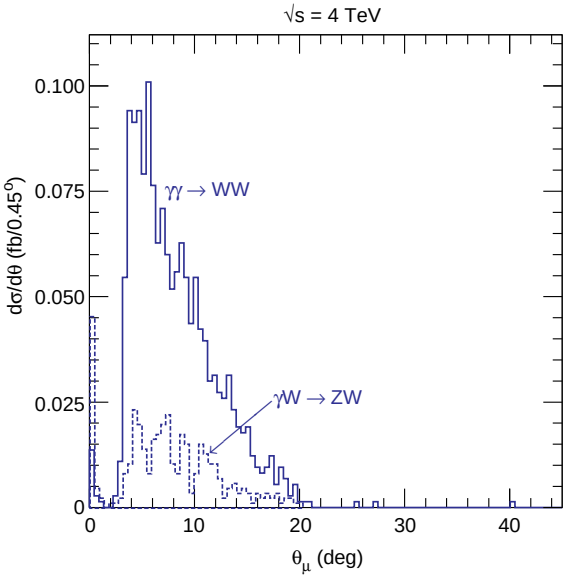

Figure 9.4: Angle of outgoing muon in $\gamma\gamma \to WW$ and $\gamma Z \to WZ$ processes after making the $p_{T,WW} > 50\,\text{GeV}$ cut described in the text.

they penetrate the cone easily and can in principle be tagged behind it. Whether this is possible in practice will, of course, depend on the muon halo, which is still being studied.

This physics simulation work is still in its infancy. As the machine related backgrounds are better understood they will be added to the simulation to see if the analysis strategy discussed above is still reasonable.

9.3 Machine Induced Backgrounds

9.3.1 Overview

A primary concern for a muon collider detector design is the level of the machine related backgrounds. There are three logically distinguishable sources; the muon halo, muon decays giving rise to high energy electrons and beam-beam interactions.

The term **muon halo** refers to those muons which are lost from the beam bunches as the muons traverse the whole collider ring. In conventional lower energy accelerators beam particles which are lost away from the intersection region are of little concern as they can be locally shielded. However 2 TeV muons can traverse kilometers of shielding so beam particle losses, almost anywhere around the machine, have the potential to generate background in the detector. The background from this source depends on a detailed knowledge of the beam profile and a credible model for beam halo and beam losses. This is not available at present. What is discussed below is a tool which is being developed to trace muons not only inside the beam pipe but also to continue this tracking outside the beam into the magnet fringe fields and shielding material. This tool will be very useful when a more detailed knowledge of the beam is known. It will eventually be necessary to devise muon spoilers and shielding for the muon halo.

With 2×10^{12} muons per bunch in the machine there are approximately 2×10^5 **muon decays** per meter giving rise to high energy electrons. The momentum distribution of these electrons follows the usual three body decay kinematics. These off-energy, off-axis electrons undergo bremsstrahlung when they traverse magnetic fields and when exiting the beam pipe interact and produce high energy electromagnetic showers and to a lesser extent hadrons and muons. Much of this debris can be locally shielded so the primary concern is muon decays near the intersection region. In the current lattice design there is a pre-focus for the beam about 130 m from the intersection point. In the discussion below it is assumed that all debris from muon decays outside this final 130 m "straight section" can be locally shielded and only decays occurring in the straight section will contribute to the machine related detector background. Much of the detector related work has been to optimize the

shielding of this final focus section and this will be discussed below. Detailed simulations of electromagnetic showers and neutron and hadron production were carried out to study the effects of various shielding strategies.

In an e^+e^- collider there is a substantial background from **beam-beam** interactions. Due to the larger muon mass, this contribution is expected to be less for a muon collider. This background contribution is considered in Chapter 8.5. Recent calculations by I.F.Ginzburg[5] and by P. Chen[6] have shown that coherent effects are not important. The classical beam-beam effects provide a smaller background than the other topics discussed here.

Since this is the first attempt to design a high energy muon collider there is a real question of how to verify the results on the backgrounds discussed here. This is compounded by the fact that there is not enough computer power to follow all the muon decays and their interactions. In an attempt to mitigate concern two very different approaches are being taken to study these problems.

One approach uses the MARS code [10] which performs fast inclusive simulations of hadronic and electromagnetic cascades, muon and low energy neutron transport in accelerator, detector and shielding components of arbitrary complexity. It has been used extensively for two decades in numerous applications at the Tevatron, UNK, SSC and LHC colliders, and for SDC, GEM, D0 and CMS detectors (for recent work see [11], [12]). The MARS code has been used from the very beginning of the muon collider study to analyze backgrounds and detector performance [11],[13],[14] as well as for calculating energy deposition in superconducting magnets, pion production, targetry and radiation issues (see other chapters). In MARS simulations all the particle interaction processes in the lattice with the detailed 3-D dipole and quadrupole geometry and magnetic field maps, in the 1.45 m radius tunnel surrounded by the soil/rock (ρ=2.24 g/cm^3), in the 26 m long and 10 m radius experimental hall and in the detector are taken into account. For background studies a 275 m section of the interaction region is considered. A single MARS run includes:

- forced $\mu \to e\nu\bar{\nu}$ decays in the beam pipe (beam muon decay studies) or beam halo interactions with the limiting aperture beam pipe;

- tracking of created electrons in the beam pipe under the influence of the magnetic field with emission of the synchrotron photons along the track;

- simulation of electromagnetic showers in the collider and detector components induced by electrons and synchrotron photons hitting the beam pipe, with appropriate hadron and prompt muon (Bethe–Heitler pairs and direct positron annihilation) production;

- simulation of muon interactions (bremsstrahlung, direct e^+e^- pair production, ionization, deep inelastic nuclear interactions and decays) along the tracks in the lattice, detector, tunnel and experimental hall components and air, and in the surrounding soil/rock;

- simulation of electromagnetic showers created in the above muon interaction vertices;

- simulation of hadronic cascades generated in muon and photon interactions, with daughter electromagnetic showers, with muon production (π and K decays, prompt muons in hadronic and electromagnetic interactions), and with low–energy neutron transport;

- histogramming and analysis of particle energy spectra, fluence and energy deposition in various detector and collider regions.

Energy thresholds are 1 MeV for muons and charged hadrons, 0.3 MeV for electrons and photons, and 0.5 eV (0.00215 eV in some cases) for neutrons.

The second approach provides a more detailed look at shower development and sources. It uses GEANT, the standard CERN high energy physics simulation tool to do all the particle tracking and it has been augmented, where necessary, with the appropriate physics processes for this muon collider study. EGS[7] was used to give full shower development for electromagnetic showers. GEANT-3.21 was used with FLUKA[8] to propagate hadronic showers and high energy γ hadron interactions and with the MICAP option[9] to transport low energy neutrons. This approach allowed for detailed studies of specific problems and a step by step approach to developing a satisfactory shielding strategy. Much of the discussion below follows the logic of the latter approach with the MARS conclusions provided for comparison purposes.

9.3.2 The Muon Halo

Beam particles which stray from the muon bunch anywhere around the collider ring, may propagate through the accelerating chamber walls, magnet yokes and other surrounding structures, and eventually reach the detector to contribute to the background. Halo muons decay and produce synchrotron radiation and secondaries, part of the overall detector background. The only practical way to control stray muons is by deflection with magnetic fields, scraping and cleanup will be done on the opposite side of the ring from the detector. Clearly to get as clean a machine as possible the bunches will have to be prepared carefully.

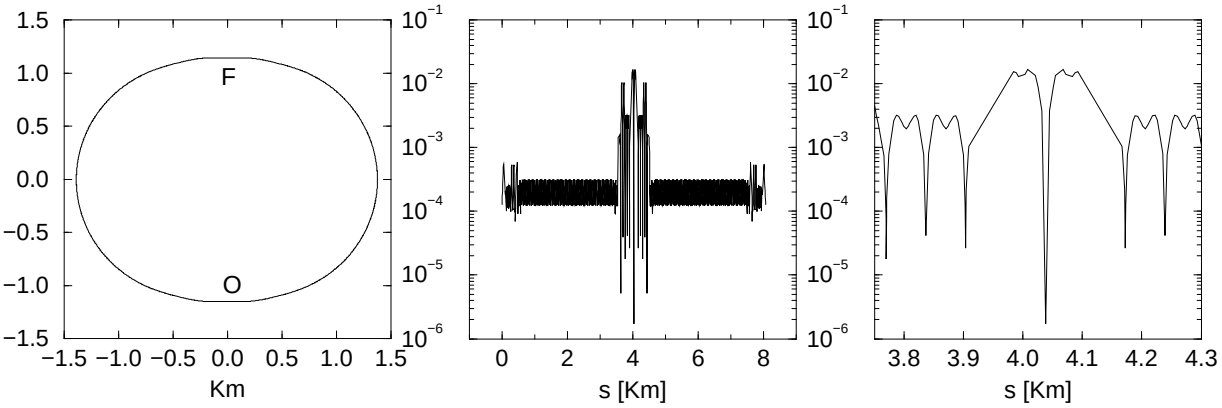

Figure 9.5: a: reference orbit for tracking from O to the final focus F in the Garren lattice. b: horizontal envelope [m] of the muon beam calculated with *Mad* for an emittance of10π $mm - mrad$. c: beam envelope [m] near the final focus.

First results on numerical tracking of the muon halo are presented here. No attempt was made to track secondaries, to optimize magnetic shields, or represent a realistic beam halo. The tracking was done by numerical integration of the equations of motion of the muons through the magnets of the collider, represented by field maps. The machine lattice is based on the work of D. Trbojevic, J. Gallardo and finally Al Garren. It will be referred to as the Garren lattice. The collider is a ring 8 km in circumference, Fig. 9.5a, with beta functions varying in wide limits in the final focus (FFC) region, F in the figure. Fig. 9.5b,c show the horizontal envelope of the beam for a normalized emittance of 10π $mm - mrad$. The lattice optics were calculated with the *Mad* code[3].

A distribution of particles in phase space is propagated starting at O in Fig. 9.5a. The algorithm used is a quasi-symplectic Predictor-Corrector with variable step; the starting step was 1 mm. The integration proceeded through field maps of dipoles and quadrupoles (super conducting RHIC type), both in the gap and in the coil and yoke regions. A third type of magnet, toroids, to be used as magnetic shield, was included for future use. This calculation assumed a field strength of $\sim$9 T.

There is a tracked reference particle, a muon starting on axis at O. The angle of deflection of this particle through the dipoles, compared with the dipole angle of *Mad*, provided the field calibration. Two reference systems of coordinates were used: system (i) relative to the reference orbit and system (ii) relative to the laboratory. System (i) shows tracked particles in the vicinity of the machine, while system (ii) was mainly used to see whether a stray particle falling out of the machine would eventually reenter it. System (i) was rotated at each dipole end, and successive dipole map slices were staggered to follow the reference

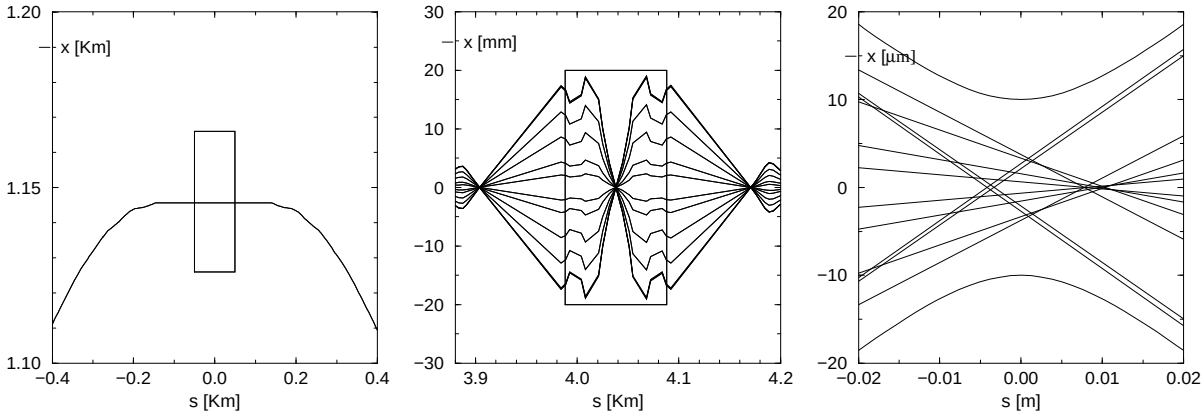

Figure 9.6: a: Reference orbit detail for the final focus showing a 20 m × 20 m detector box. b: Colliding muons (accepted) in the box. Some orbits are shown ; step every 0.15 μrad in the starting angle c: Blow-up of the central part of the previous figure showing the final focus.

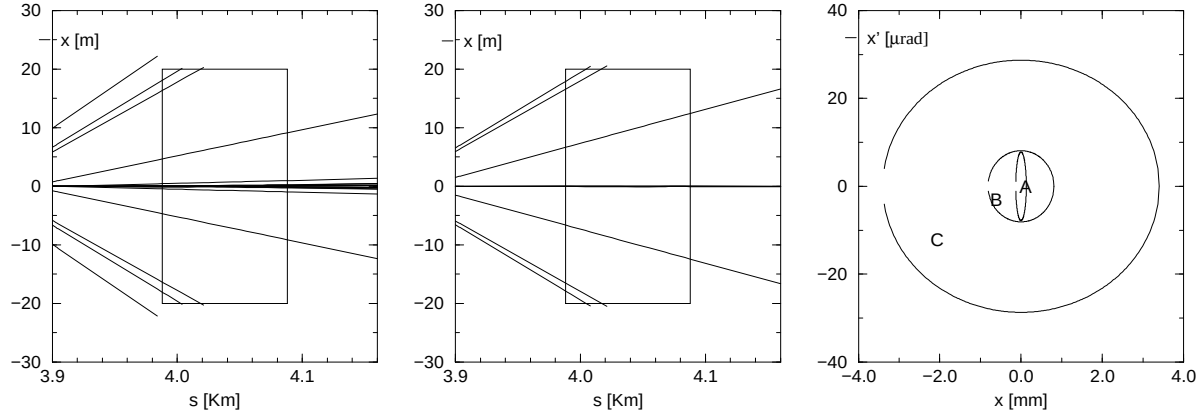

Figure 9.7: a,b: Final focus orbits for background muons relative to the detector box, for various initial angles and positions. c: Phase space acceptance (and halo). B are accepted, C are *not* accepted.

trajectory. It is an unusual tracking. Generally, one tracks particles *inside* an accelerator. Here, the tracking is mostly on the *outside*.

The Final Focus (FFC) region with a nominal 20 m $\times$ 20 m detector box is shown in Fig. 9.6a. Fig. 9.6b shows the trajectories of muons that are accepted by the lattice and will propagate in the collider. These well behaved muons produce the beam at the intersection point for which the machine is being designed. Fig. 9.6c is a blow-up of the FFC, with trajectories and their envelope shown.

Fig. 9.7a,b shows some badly behaved muons, i.e. muons that propagate through magnet yokes and coils and escape the lattice in the FFC, where the fast oscillations of the machine functions shake them off. These muons impinge on the detector box. They are the background halo.

The initial muon distribution used in the calculations is shown in the diagram of Fig. 9.7c, in the horizontal plane (a similar one holds for the vertical). The A ellipse represents the machine acceptance calculated from *Mad* beta for a normalized emittance of $10\pi\ mm-mrad$. The B ellipse contains the well behaved muon beam of Fig. 9.6b. The region between the contours of B and C contains the bad halo muons of Fig. 9.7a,b. Muons outside C are soon lost for good, generally when they encounter the first difficulties with the lattice bends.

Clearly the work discussed here has the potential to significantly contribute to the detailed design of the muon collider. With the addition of muon energy loss and muon decay probabilities, this tool will help not only to predict detector backgrounds from halo muons but also to aid in the design of muon spoilers to reduce the potential halo background in the detector.

9.3.3 Design of the Intersection Region

The current design of the Intersection Region is driven by the desire to reduce the background from muon decays in the detector as much as possible. For this study the 130 m final focus section (Fig. 9.8) which includes the final four quadrupoles, three toroids, a 2 Tesla solenoidal field for the detector and the connecting beam pipe and shielding was modeled in GEANT (Fig. 9.9) with all the appropriate magnetic fields and shielding materials. Studies of the effects of high energy electrons hitting specific edges and surfaces were carried out and the shielding adjusted or augmented to mitigate the apparent effects of particular background problems. Effects due to electrons, photons, neutrons and charged hadrons and muons were considered in turn to try to optimized the design. While the current design is not fully optimized, it is a marked improvement over a much simpler design which had been used in the past. More importantly, it helped develop the tools and strategy to do such an

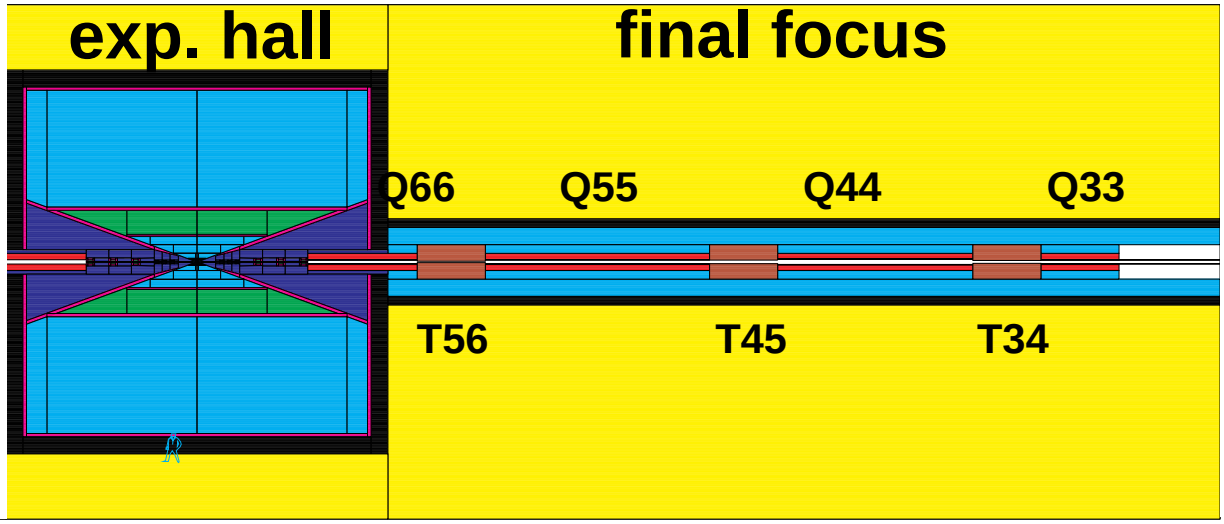

Figure 9.8: Region around the Intersection Region modeled in GEANT. The black regions represent tungsten shielding. The final quadrupoles (Q) and toroids (T) on one side of the detector enclosure are shown. The shaded areas around the intersection point represent the various detector volumes used in calculating particle fluences.

optimization as the lattice is further developed.

The final focus may be thought to be composed of 3 separate regions. The longest of these, from 130 m to approximately 6.5 m contains the quadrupole magnets which bring the beam to the final focus in the intersection region. The space available between the four quadrupoles was used to install toroids. They fulfill a double role: first they are used as scrapers for the electromagnetic debris; secondly, they serve as magnetic deflectors for the Bethe–Heitler(BH) muons generated upstream. The effect of the toroids on the BH muons will be discussed later. In order to optimize the inner aperture of the toroids, the σ_x and σ_y envelope of the muon bunch at every exit of the quadrupoles has been estimated. The inner aperture of each toroid was chosen to match the 4 σ ellipse of the muon bunch at that point. For example, Fig. 9.10 represents the the xy envelope of the muon bunch at the exit of Q55. Similarly, Fig. 9.11 shows the same distribution for the decay electrons. Fig. 9.12 and Fig. 9.13 show the y projection of the above envelopes.

The second region, from 6.5 m to 1.1 m contains tungsten plus additional shielding boxes to help contain neutrons produced by photons in the electromagnetic showers (Fig. 9.14). A shielding box consists of a block of Cu surrounded by polyboron. The shielding here is designed with inverted cones to reduce the probability of electrons hitting the edges of collimators or glancing off shielding surfaces (Fig. 9.15). The beam aperture at the entrance to this section is reduced to 2.5 cm and by the exit of the section to 4.5 mm. This profile

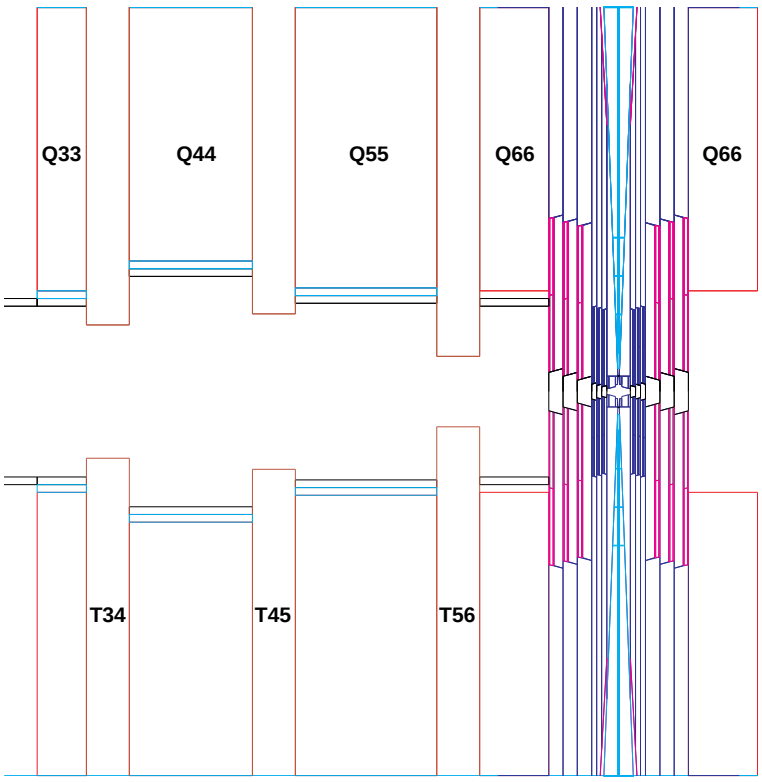

Figure 9.9: GEANT description of the Intersection Region. The horizontal scale is 100 m while the vertical is only about 5 cm. The shapes in the figure are the actual GEANT surfaces used in the simulation. Q represents a quadrupole and T a toroid magnet.

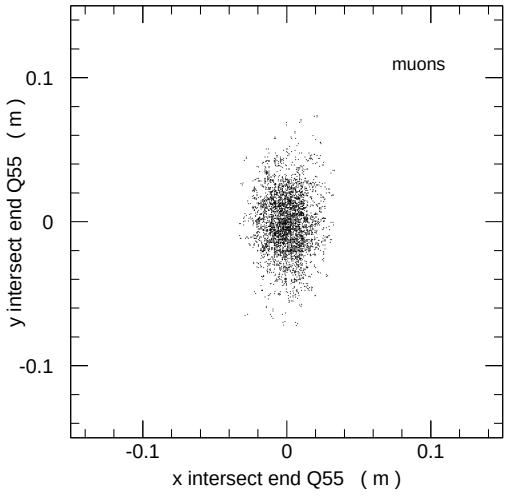

Figure 9.10: The xy envelope of the muon bunch at the exit of Q55.

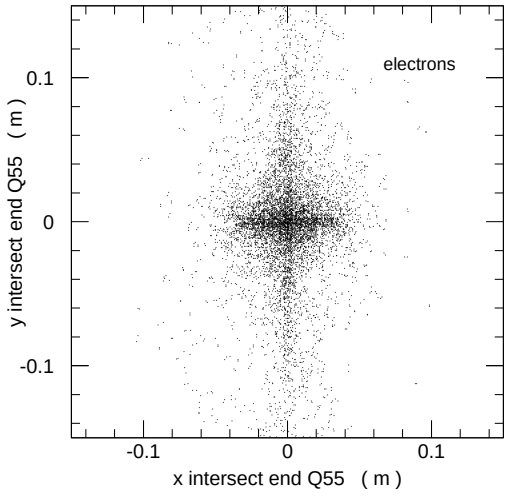

Figure 9.11: The xy envelope of the decay electrons at the exit of Q55.

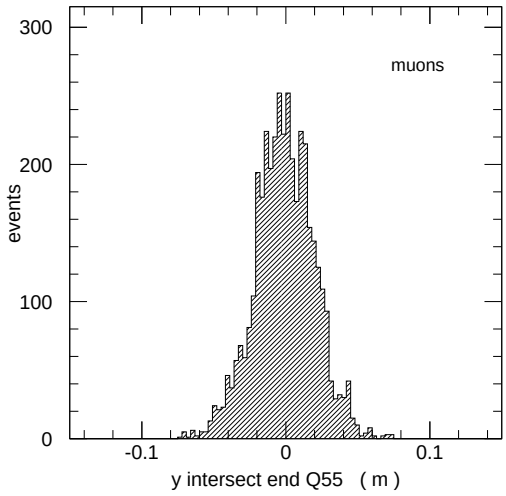

Figure 9.12: The y projection of the muon bunch at the exit of Q55.

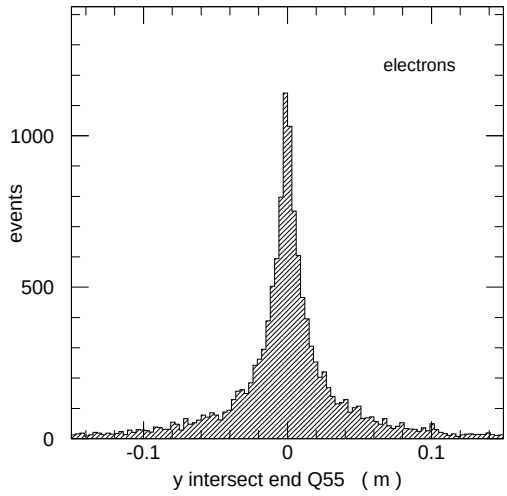

Figure 9.13: The y projection of the decay electrons at the exit of Q55.

follows the beam envelope as the particles approach the intersection region. The intersection region itself (Fig. 9.16) is designed as an inverse cone to prevent electrons which reach this region from hitting any shielding as this region is directly viewed by the detector. Approximately 2% of the electrons from muon decays in the final 130 m around the intersection point interact with shielding in the intersection region, 30% in the adjacent region, 58% in the outermost region where the final quadrupoles exist and the other 10% pass right through the region without hitting any shielding.

A 20° tungsten cone around the intersection region is required for the reduction of the electromagnetic component of the background. The cone is lined, except very near the intersection region with polyboron to reduce the slow neutron flux. In the shielding calculations it is also assumed that there is a polyboron layer before the calorimeter and surrounding the muon system. In earlier designs this cone was only 9°. Whether or not the full 20° is required is still under study and work is ongoing to evaluate the physics impact of this choice of the shielding cone angle. It is likely that, after optimization is completed, the cone angle will be reduced.

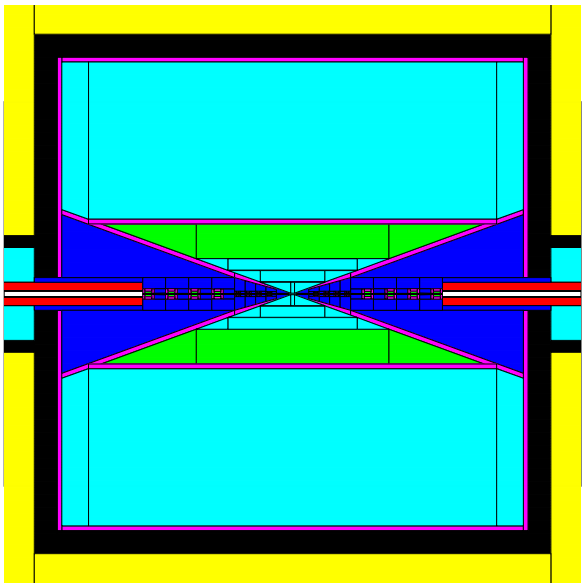

Figure 9.14: Detail near Intersection region. The final 10 meters on either side of the intersection point are shown. The dark regions are tungsten while the detector volumes are the shaded regions around the intersection point. The lighter region around the tungsten represent the polyboron for neutron absorption. The sections to reduce the neutrons can be seen as the boxes along the beamline decreasing in size as they approach the intersection point.

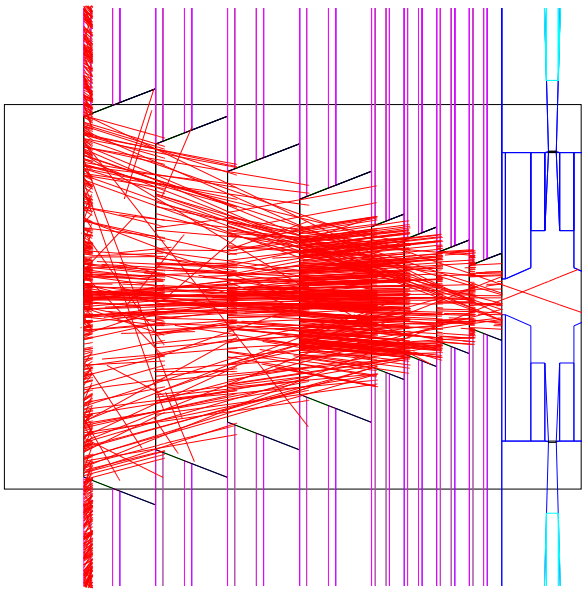

Figure 9.15: Expanded View of Region (2) near the Intersection point. The lines represent electrons from a random sample of muon decays.

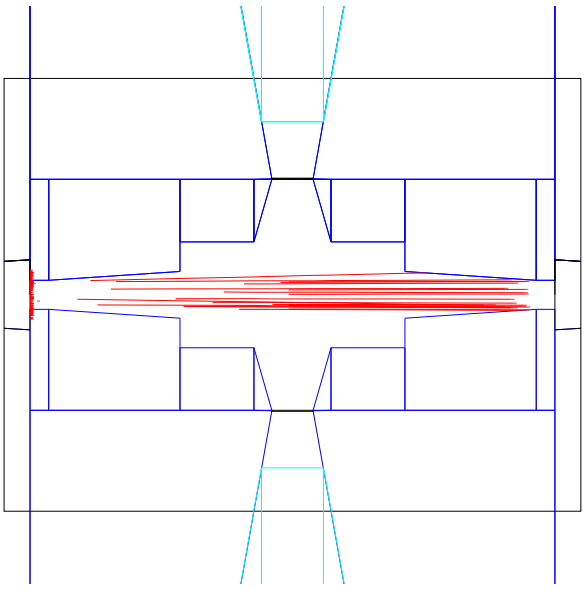

Figure 9.16: Detailed View of Region (1), the Intersection Region. The lines represent electrons from a random sample of muon decays.

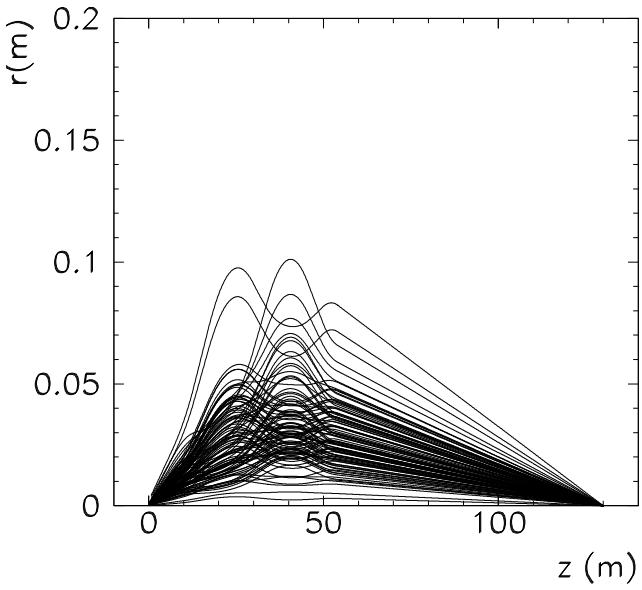

Figure 9.17: Muon Trajectories in the Final Focus Region with Muon decays turned off

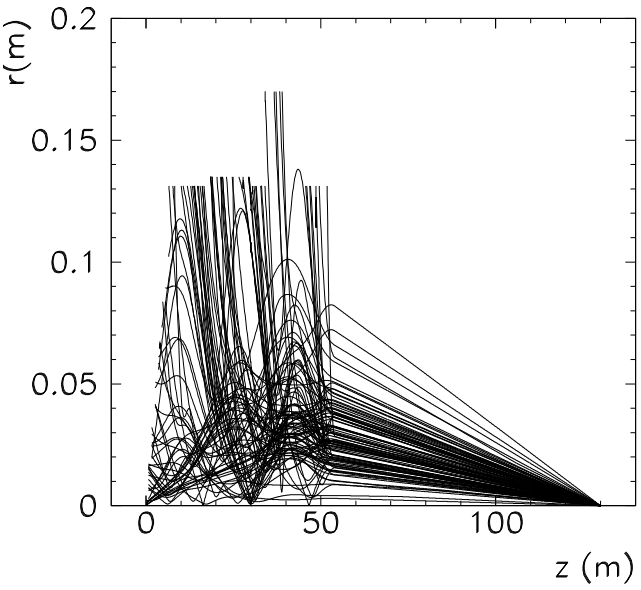

Figure 9.18: Muon Trajectories in the Final Focus Region with Muon Decays allowed. The decay electrons are tracked until they reach either a magnet or shielding.

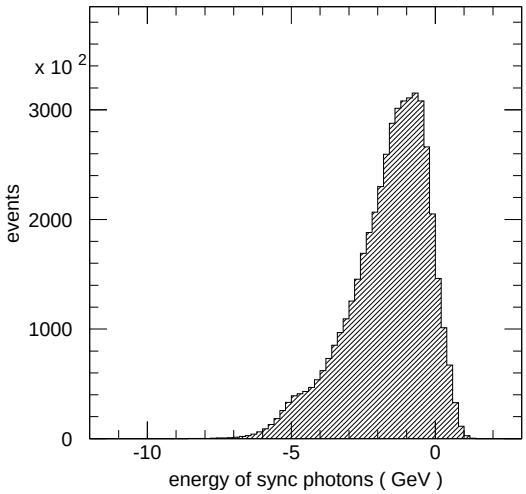

Figure 9.19: Log of the energy of synchrotron radiation photons.

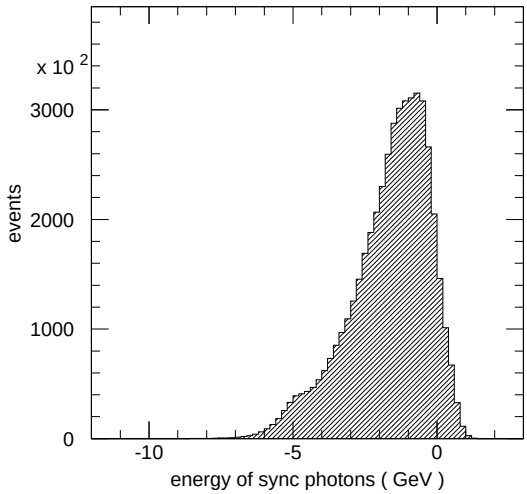

Figure 9.20: Log of the critical energy.

9.3.4 Muon Decay Backgrounds

Results using GEANT Simulation

The primary source of machine related background in the detector is muon decays in the straight section near the intersection region. The trajectory of muons, assuming they do not decay, approaching the final focus is shown in Fig. 9.17. When decays are included (Fig. 9.18) the decay electrons essentially follow the parent muon trajectory in the field free region but when they enter the final focus quadrupoles they are sprayed off-axis and eventually hit the magnets, beam pipe and other shielding.

These high energy electrons shower to produce not only electrons and photons but to eventually produce to a much lesser extent neutrons and other charged and neutral hadrons and even muons.

The backgrounds in the detector are defined as the fluence of particles (number of particles per cm^2 per beam crossing) across surfaces which are representative of the various kinds of detectors which might be considered. For this study the calorimeter was assumed to be a composition of copper and liquid argon in equal parts by volume which represents a good resolution calorimeter with approximately 20% sampling fraction. The other volumes of the detector were vacuum. The calorimeter starts from a radius of 150 cm and is 150 cm deep. The tracker volume is defined from 50 to 150 cm . An array of horizontal and vertical planes were placed in the detector volumes. These planes were used for flux calculations; their

positions are evident in the tables of rates below.

A number of specific backgrounds have been considered at this point. **Bremsstrahlung** from the primary muons has been calculate and, as one would suspect, makes little contribution to the final background in the detector.

The **electromagnetic showers** generated by the decay electrons are fully tracked through GEANT. The present simulation has an electron and a photon cutoff at 25 keV. The mean photon energy is 1 MeV. Due to the 2 T field, all electrons are confined to a very small radius. The soft photon flux has a small probability of producing uncorrelated hits in the tracking chambers, but mostly deposits energy in the electromagnetic calorimeter. As one can see from Fig. 9.18, the electrons can reach rather large distances from the beam axis, resulting in substantial synchrotron radiation in the high field regions of the quadrupoles. Every electron radiates on average 300 photons. The average critical energy is 700 MeV and the average energy of the photons is 500 MeV. The respective distributions can be seen in Fig. 9.19 and Fig. 9.20. The total energy carried by the synchrotron radiation amounts to 20% of the initial average energy of the electron. Because of the small energy carried by the synchrotron photons and the fact that they do not point well toward the small opening of the shield at the intersection region, the contribution of the synchrotron radiation photons is small.

One electron generated background of concern is **Bethe-Heitler muon pairs**. Even though the pairs are in general created near the initial electron impact point, the muons can penetrate the shielding to reach the detector. The photo-pair production of muons by electrons impinging on heavy targets were simulated according to Y.S. Tsai[15]. The probability of an electron to generate a muon on a thick tungsten target is shown in Fig. 9.21 as a function of electron energy. The average muon momentum produced by a 500 GeV electron is 17 GeV and the distribution is shown in Fig. 9.22. The momentum distribution of the generated Bethe Heitler muons in the whole final focus region is shown in Fig. 9.23. The average momentum is 27 GeV and the average probability for an electron to produce such a muon is $5.6{\times}10^{-4}$.

Fig. 9.24 shows the GEANT tracing of 50 Bethe–Heitler muons. All the magnetic fields were active: the quadrupoles, the field in the return yoke of the quadrupoles, the three toroids with peak B-ϕ fields of 4, -4, and 4 T. The experimental cavity had a solenoidal field of 2 T. Ionization losses occur in all the materials (metal, the ground, concrete walls, etc...) and decays are allowed. While the beneficial role of the toroids is clear, lower energy muons are bent away from the vertex and the tracker volumes, optimization will be needed.

Many Bethe–Heitler muons will cross the calorimeter and catastrophic bremsstrahlung losses could cause spikes in the energy distribution. Fig. 9.25 shows the energy distribution

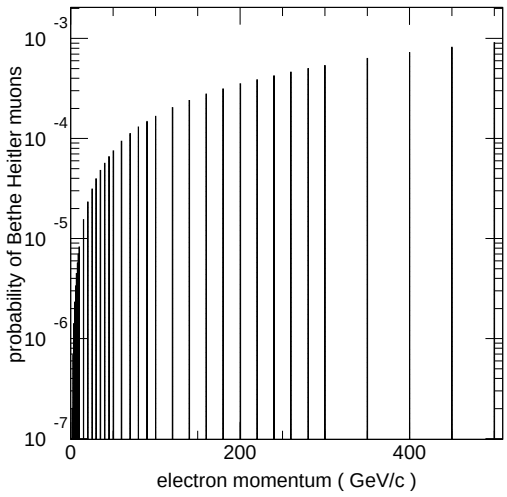

Figure 9.21: Probability of an electron to generate a muon on a thick tungsten target.

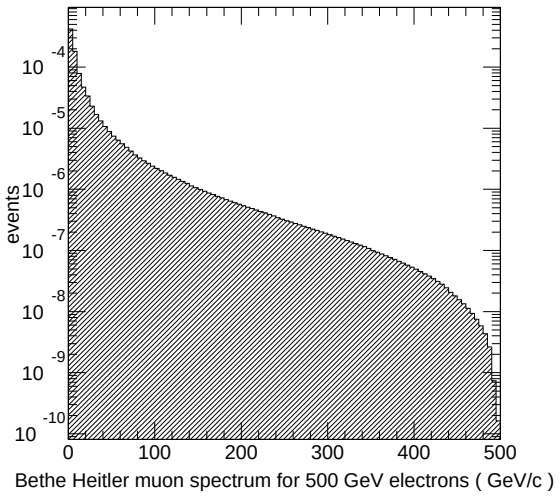

Figure 9.22: Muon momentum spectrum produced by a 500 GeV electron.

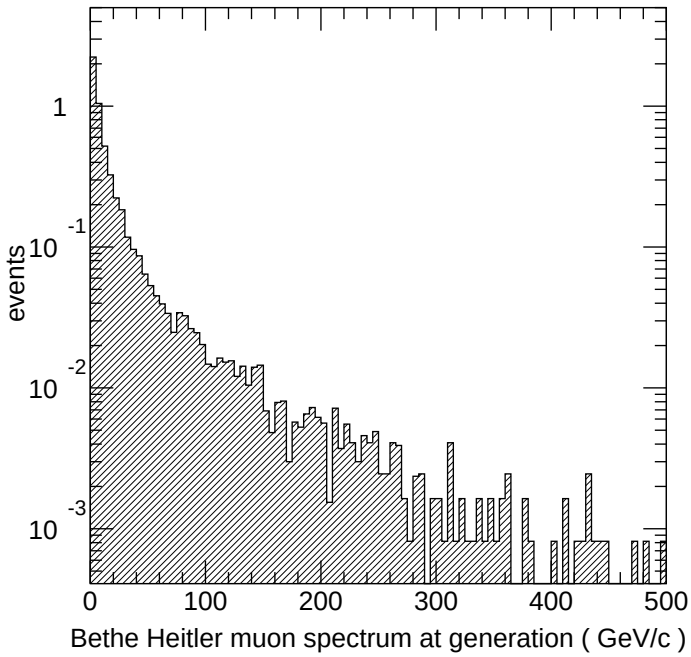

Figure 9.23: Bethe-Heitler muon spectrum in the final focus region.

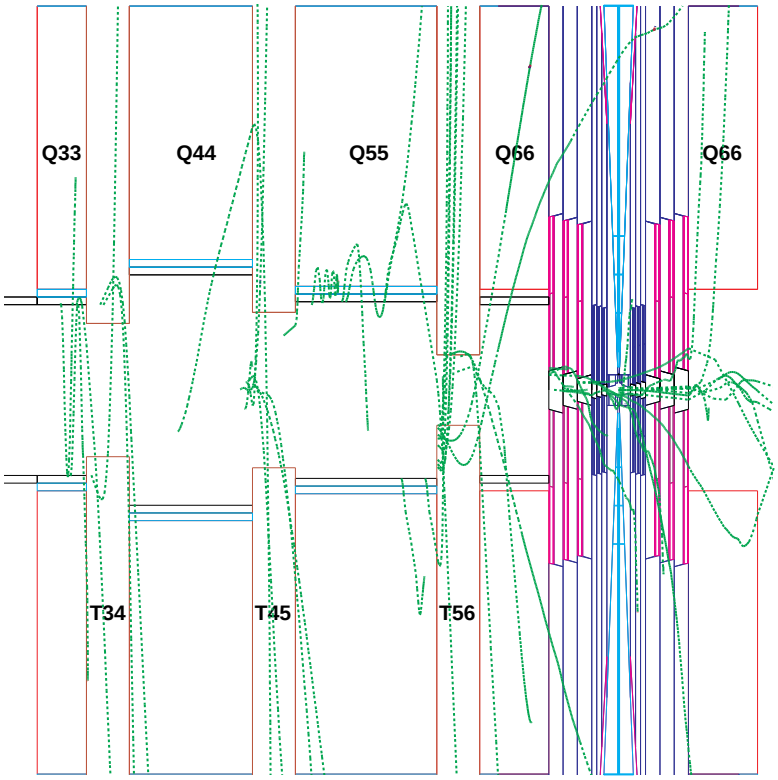

Figure 9.24: Tracing of Bethe-Heitler muons by GEANT.

in the calorimeter, as a function , integrated over r, of z and ϕ, due to Bethe–Heitler muons in a single crossing of 2 bunches of 10^{12} muons each. The energy spikes can be easily identified by the abnormal longitudinal profile of the shower. Nevertheless, it will impose constraints on the calorimetric performance which can be achieved. It is clear that good longitudinal segmentation will be required.

A major effort has been directed towards understanding the **hadron background** in the detector. The hadrons come primarily from photon interactions in the shielding. While the probability of photoproduction of hadrons is quite small relative to other processes the large number of photons released per crossing and their high initial energies make this an important background issue. The relevant photon energy range and the relative cross sections for different processes are illustrated in Fig. 9.26. In the few MeV region (5 MeV - 150 MeV) the preferred models have the photon interacting with the nucleus as a whole (Giant Dipole Resonance) or with a component of the nucleus (Quasi-Deuteron Region). In both these regions the photon shakes free one or more (more than one about 20% of the time) neutrons. In the present model only one neutron is released with the appropriate energy and angular distribution. In practice, just as many protons are released, but since their kinetic energy is low, they are ignored at present. The region from 150 MeV to about

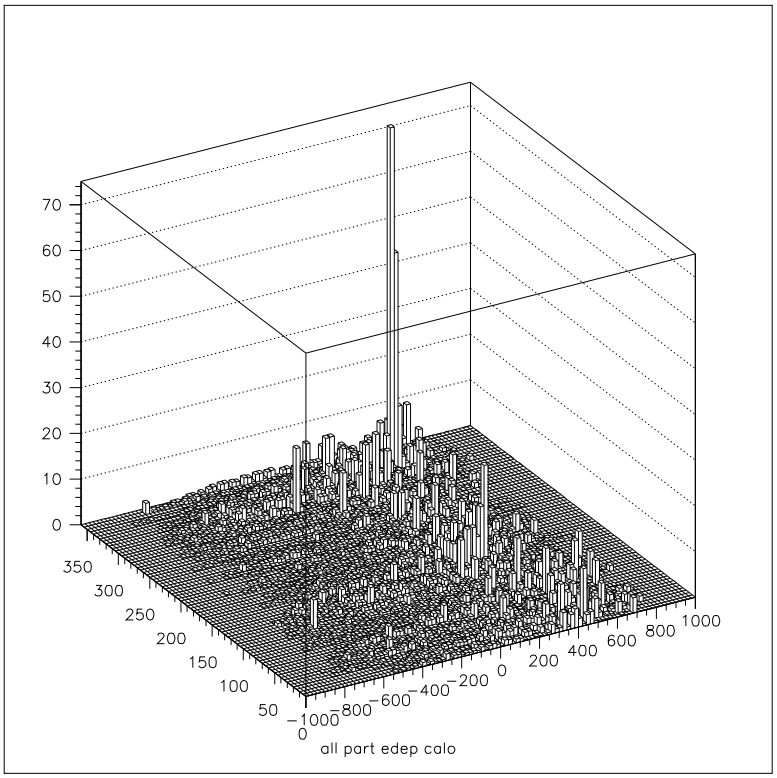

Figure 9.25: Energy distribution of Bethe–Heitler muons as a function of ϕ and z in the calorimeter. Only muons from interactions from one beam are shown.

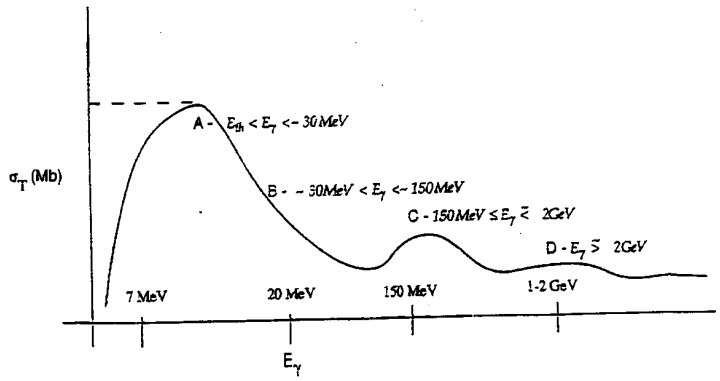

Figure 9.26: Cross section for photoproduction of hadrons.

2 GeV is the resonance region which is presently modeled as the production and decay of an N*. At higher energies vector dominance is assumed and a ρ meson decaying into pions is modeled. The present approximations are thought to give a reasonable representation of the number and spectrum of hadrons from the calculated photon flux. All the photons resulting from nuclear de-excitation were ignored.

A typical high energy (650 GeV) electron hitting a tungsten collimator produces initially, on average, 266 neutrons of average kinetic energy 2.9 MeV, 2.6 N* and 1.1 ρ mesons. Few of the neutrons reach the detector. However due to rescattering, the number of neutrons in the detector region per crossing is in the thousands. The momentum distributions of neutrons at generation and in the detector region per crossing are shown in Fig. 9.27 and Fig. 9.28 respectively. The initial kinetic energy of neutrons from the giant dipole source is .003 GeV, while the initial kinetic energy of neutrons and protons from the resonance region is .09 GeV and the average momentum of the generated pions is .75 GeV/c.

In figure Fig. 9.29 the neutron background is shown in the xz plane, and in Fig. 9.30 in the plane perpendicular to the z axis at the intersection point. These pictures are for 5 separate 1 Tev electrons impinging on the tungsten shield at a distance of 110 cm from the IP. Only the neutrons are shown in the figures.

In figure Fig. 9.31 and Fig. 9.32 the charged hadron backgrounds in the same two projections are shown. In this case 500 separate 1 Tev electrons were generated. The pictures are dominated by the large number of recoil protons kicked off the polyboron shield by energetic neutrons. The average momentum of the protons is only 200 MeV and this particular background can probably be suppressed by a layer of metal covering the polyboron shield. The flux of recoil protons is reduced by a factor of 3 when a 20 ns gate is applied. The average momentum of the pions is 240 MeV.

Some of the background particles are non-relativistic and/or are generated far away from the intersection point. Fig. 9.33 shows the time of generation of the slowest background particles: the neutrons. The remaining background from the previous bunch crossings is at the level of 0.1% for the whole final focus region and is at the level of 1% for the tracker/vertex volume, Fig. 9.34. (assuming a bunch crossing every 10-20 μ)

A summary of the backgrounds from muon decay is given in Table 9.1, Table 9.2 and Fig. 9.35, where the fluences for the various backgrounds as a function of detector radius are shown. In order to facilitate the positioning and the orientation of the detectors, two types of fluences have been calculated: radial where the particle traverses a cylinder parallel to the beam axis and longitudinal, where the particles traverse a plane perpendicular to the beam axis at the interaction point (z=0). The fluences at a given radius are similar in both cases reflecting the fact that most of the particles are very soft. All the fluxes are integrated

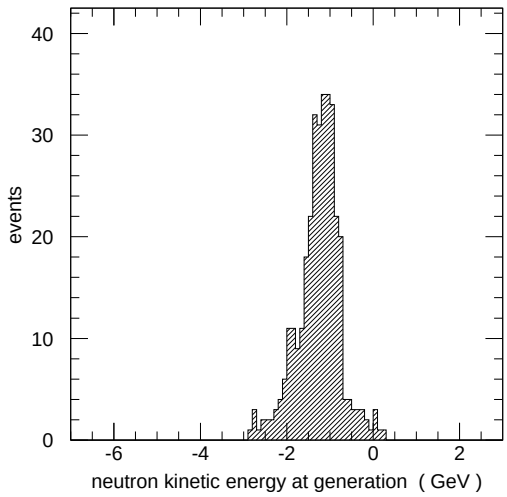

Figure 9.27: Log of generated neutron energy spectrum.

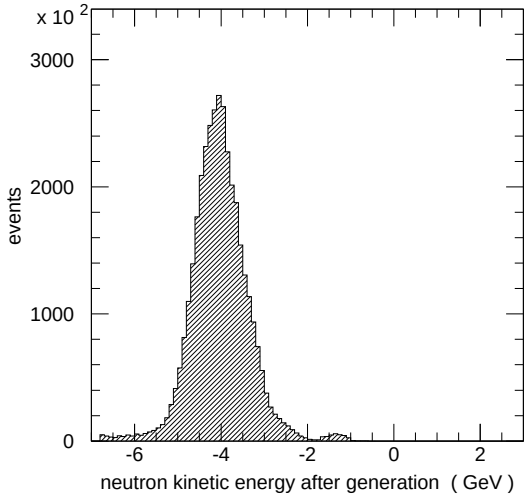

Figure 9.28: Log of neutron energy in the detector region.

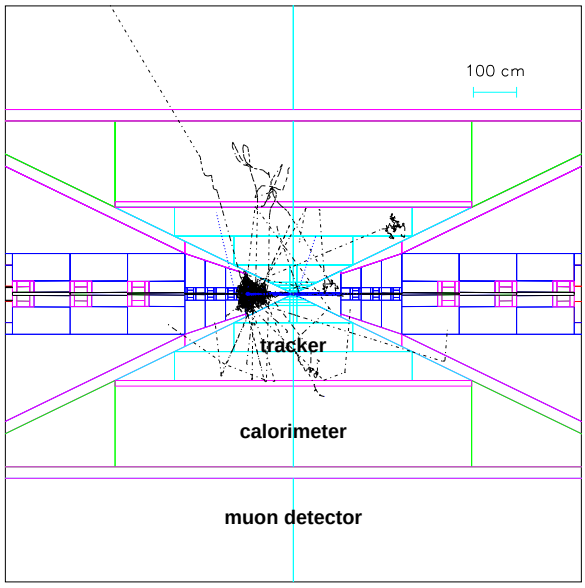

Figure 9.29: Neutron distribution in xz plane.

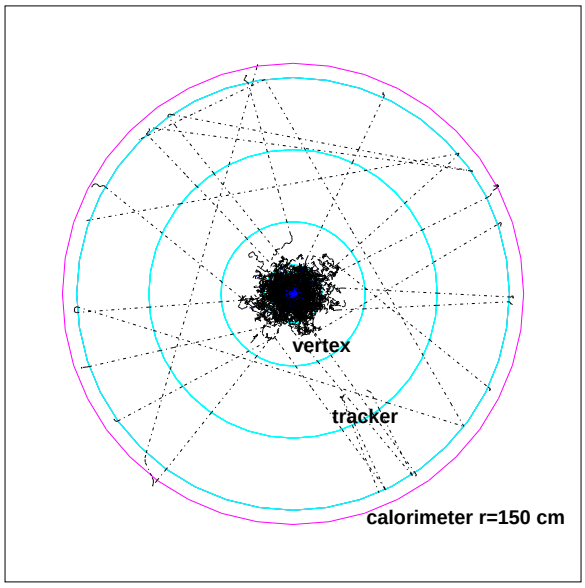

Figure 9.30: Neutron distribution normal to beams at z=0.

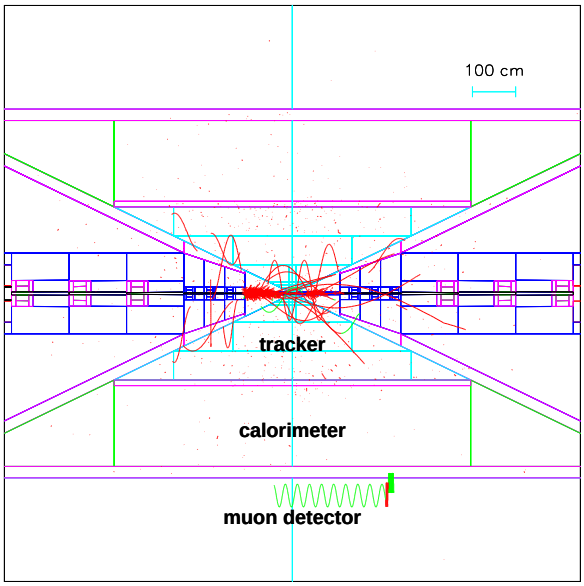

Figure 9.31: Charged hadron distribution in xz plane.

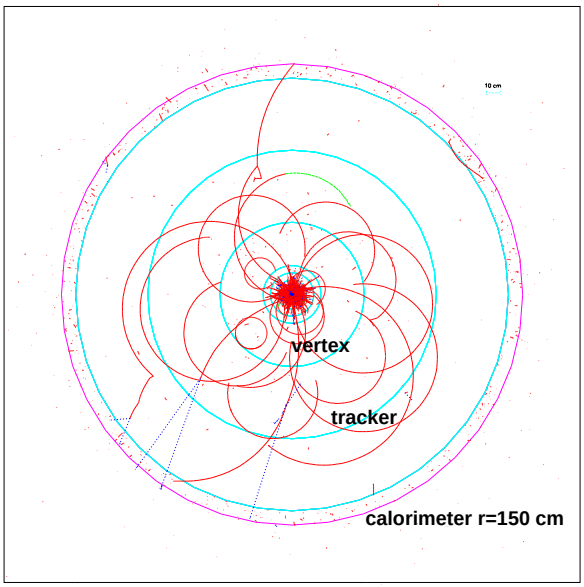

Figure 9.32: Charged hadron distribution normal to beams at z=0.

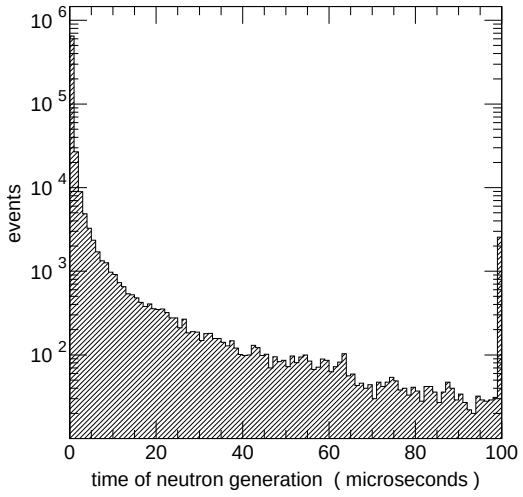

Figure 9.33: Time spectrum of the neutron background.

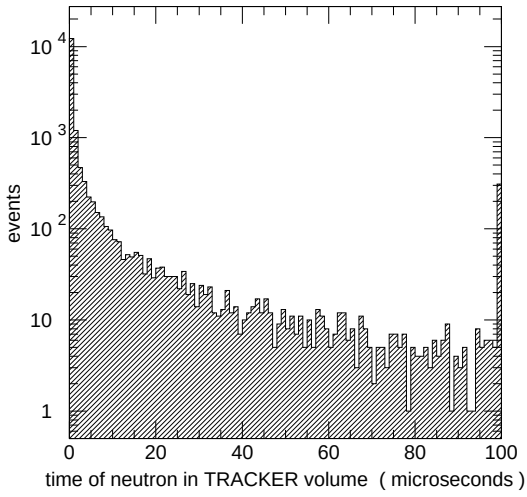

Figure 9.34: Time spectrum of neutrons into the tracker.

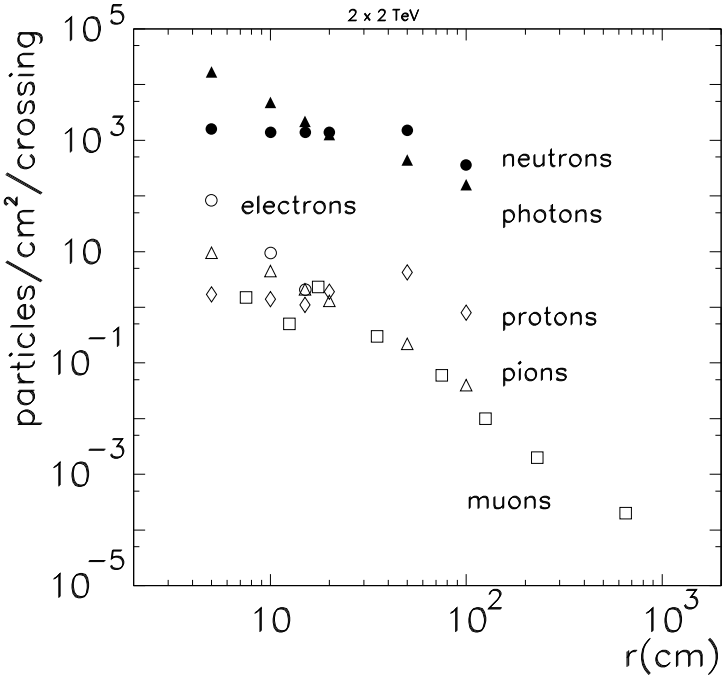

Figure 9.35: Particle fluences as a function of raduius.

over 20 μs. Only the proton and neutron fluxes are affected by timing cuts of the order of 20 ns. No significant differences were observed for integration times of 2 μs and 10 μs.A word of caution : in order to be able to compare our backgrounds with the ones calculated by MARS code or the ones predicted for NLC , all the values in Table 9.1, Table 9.2 and Fig. 9.35 apply for the crossing of two bunches of $10^{12}\mu$'s each . The average energies of the particles are given in Table 9.3.

With the present design the total energy deposited in the calorimeter is 427 TeV. The main contributors are the soft electromagnetic component (13 Tev), the hadronic byproducts of the electromagnetic shower (411 TeV) and the energy deposited by the Bethe– Heitler muons with their occasional catastrophic bremsstrahlung (3.4 TeV for a 4 Tesla toroidal field). The last component is not uniformly distributed in the calorimeter and imposes limits on jets measurements . In the absence of toroids, the muons deposit only 2.7 TeV in the calorimeter while for a toroidal field of 8 Tesla , the amount of energy deposited grows to 5.9 TeV .

Table 9.1: Longitudinal Particle Fluences from Muon Decays and Interactions from the GEANT Calculation. Fluence = particles/cm^2/crossing for two bunches of $10^{12}\mu$'s each.

Detector	Radius(cm)	γ's	neutrons	$e^{\pm}$	$\pi^{\pm}$	protons	$\mu^{\pm}$
Vertex	5-10	7900	1100	69	14.4	0.8	1.5
	10-15	3100	1200		3.7	0.05	0.5
	15-20	1600	1000		4.6	4.0	2.3
Tracker	20-50	450	870		0.8	3.9	0.3
	50-100	120	520		0.1	2.2	0.06
	100-150	130	330		0.003	0.4	0.01
Calorimeter	160-310						0.002
Muon	310-10000						0.0002

Table 9.2: Radial Particle Fluences from Muon Decays and Interactions from the GEANT Calculation. Fluence = particles/cm^2/crossing for two bunches of $10^{12}\mu$'s each.

Detector	Radius(cm)	γ's	neutrons	$e^{\pm}$	$\pi^{\pm}$	protons	$\mu^{\pm}$
Vertex	5	16900	1600	84.0	9.5	1.7	.35
	10	4800	1400	9.4	4.5	1.4	0.43
	15	2200	1400	2.1	2.1	1.1	0.33
	20	1250	1400		1.3	1.9	0.20
Tracker	50	440	1500		0.22	4.2	0.032
	100	160	360		0.04	0.8	0.008

Results from MARS

Similar calculations have been carried out using the MARS code. At present the intersection region being used here is quite different from the one used in the GEANT simulation discussed

Table 9.3: Mean kinetic energies and momenta of particles as calculated by GEANT.

Particle	γ	p	$\pi^{\pm}$	n
$\langle$Kinetic E$\rangle$, MeV	1	30	240	10

Detector	Radius	μ momentum from Bethe–Heitler(GeV)	μ momentum from π decay
Vertex	10-20	24	
Tracker	50-100	66	0.13
	100-150	31	
Calorimeter	160-310	19	

above. In particular the shielding cone is only 9°.

Fig. 9.36 shows the muon flux entering the interaction region toward the detector. There is a noticeable rate across the entire detector. Fig. 9.37 shows the formation of long range particle fluxes in the 275 m interaction region: lattice components, tunnel and experimental hall air, surrounding soil/rock, and detector components are simulated with the interaction point at 10 m.

Particle fluxes in the central detector are shown in Fig. 9.38. There is a rather uniform distribution of neutrals in the cavity with charged fluxes almost three orders of magnitude lower. Mean energies of those particles in the inner tracker are given in Table 9.4

Table 9.4: Mean energies of particles in inner tracker for 2 TeV μ^+ decays in the interaction region as calculated with MARS.

Particle	γ	$e^\pm$	$h^\pm$	n	μ
$\langle$E$\rangle$, MeV	2.5	80	249	0.2	3630

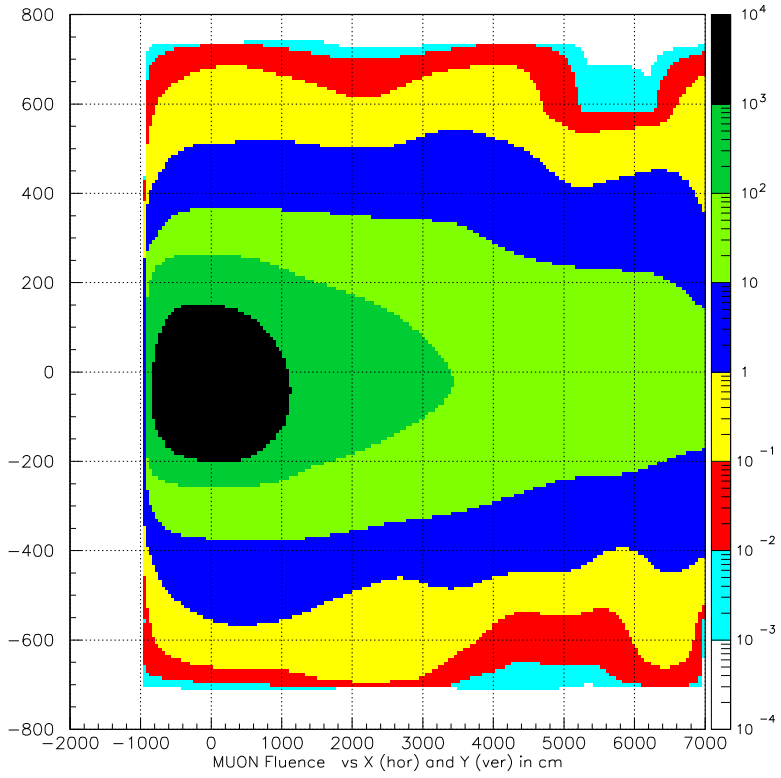

Figure 9.36: Muon flux contours ($cm^{-2}s^{-1}$) in a vertical plane of the collider tunnel and surrounding soil/rock at the entrance to the interaction region for 2 TeV muon beam decays as calculated with MARS. Beam axis is at x=y=0.

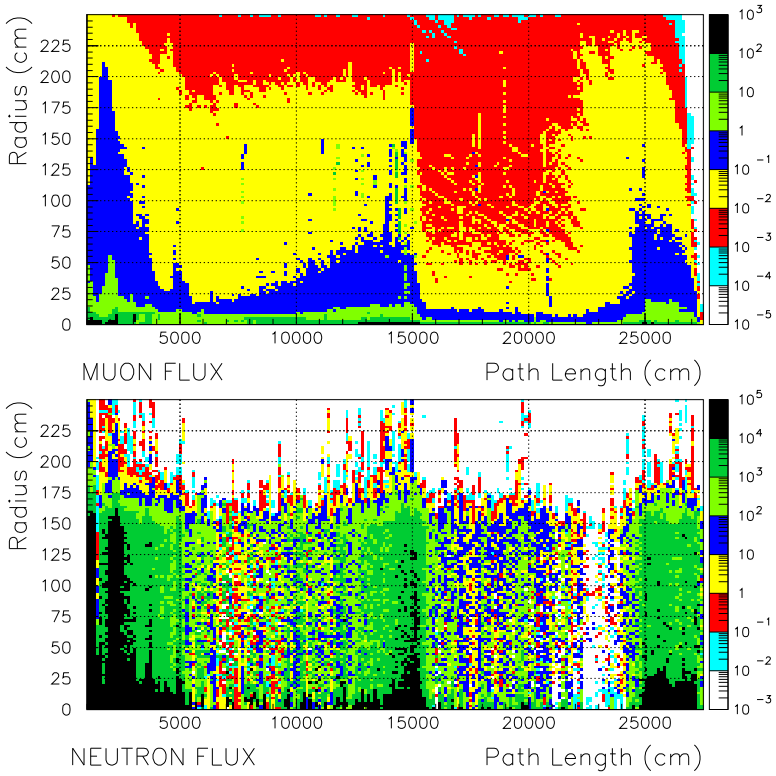

Figure 9.37: Muon (top) and neutron (bottom) flux contours ($cm^{-2}s^{-1}$) in tunnel, detector and surrounding soil/rock for 2 TeV muon beam decays as calculated with MARS. IP is at L=10 m.

9.4 Detector Specifications and Design

The physics requirements of a muon collider detector are similar to those of an electron collider. The main difference has to do with the machine related backgrounds and the added shielding that is needed near the beam pipe.

At this time little detailed work has been done on the design of a detector. Most of the discussion has centered around the types of detectors which might function well in this environment. The background levels detailed in the previous section are much higher than the comparable levels calculated for the SSC detectors and appear to be in excess of the levels expected at the LHC. Clearly segmentation is the key to successfully dealing with this environment. One major advantage of this muon collider over high energy hadron colliders is the long time between beam crossings; the LHC will have crossings every 25 ns compared to the 10 μs expected for the 4 TeV μ-collider. Much of the detector discussion has focused on ways to exploit this time between crossings to increase the segmentation while holding the number of readout elements to manageable levels.

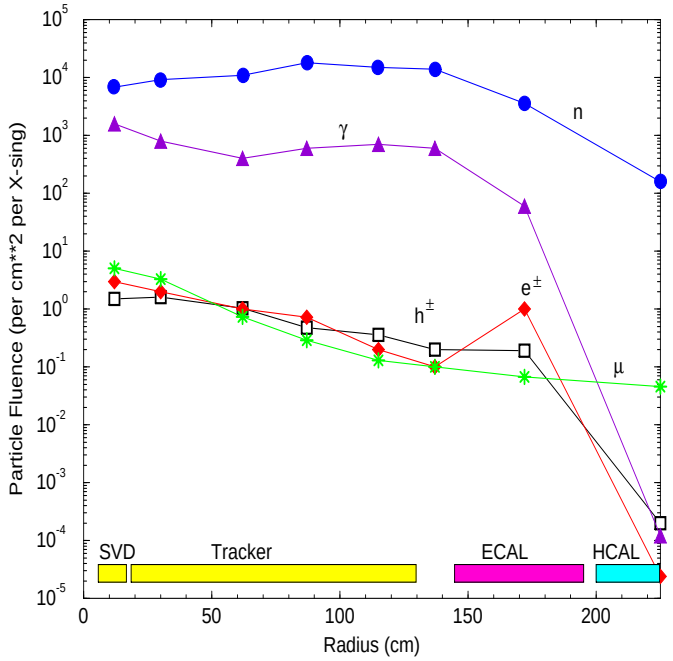

Figure 9.38: Particle flux radial distributions in a ± 1.2 m central detector region per bunch crossing due to 2 TeV muon decays in both beams as calculated with the MARS code.

While there is some detailed discussion of specific technologies below, the conceptual state of the detector design can be summarized as follows. The machine related backgrounds in the muon system behind the calorimeter are minimal. The issue for muon measurements in therefore to what extent track information from the inner tracking is required to obtain the required momentum precision. To the extent that the vertex point plus a track in the outside chambers is adequate, there is no real background issue to deal with. Much the same conclusion applies to the calorimeter system. Concerns about radiation damage and the high granularity that seems to be an advantage might necessitate a liquid electromagnetic system. The study of strong WW scattering requires very good hadron resolution to separate W and Z particles decaying into jets and reasonably precise p_T cuts on the WW system.

The real impact of the backgrounds will be felt in the inner tracking and vertex systems. One attractive possibility for a tracking system is a Time Projection Chamber[16]. This is an example of a low density, high precision device which takes advantage of the long time between crossings to provide low background and high segmentation with credible readout capability. A more detailed discussion of the use of such a device in a muon collider environment is given below. Silicon appears to be an adequate option for vertex detection.

Table 9.5: Detector Performance Requirements.

Detector Component	Minimum Resolution/Characteristics
Magnetic Field	Solenoid; B$\geq$2 T
Vertex Detector	b-tagging, small pixels
Tracking	$\Delta p/p^2 \sim 1\times10^{-3}(GeV)^{-1}$ at large p High granularity
EM Calorimeter	$\Delta E/E\sim 10\%/\sqrt{E}\oplus 0.7\%$ Granularity: longitudinal and transverse Active depth: 24 X_0
Hadron Calorimeter	Δ E/E$\sim 50\%/\sqrt{E}\oplus 2\%$ Granularity: longitudinal and transverse Total depth (EM + HAD)$\sim 7\lambda$
Muon Spectrometer	$\Delta p/p \sim 20\%$ 1 TeV

Again, because of the time between beam crossings, an attractive option here is the Silicon Drift Detector[17] and this is also discussed in detail below. It should be noted that the present backgrounds are quoted for an inner vertex detector radius of 10 cm. Work is ongoing to decide how close to the intersection point one can place this detector and still have relatively low occupancy. Given the large low energy photon flux in this region it is possible that tracking with the vertex detector is not practical because of the resulting large combinatorial problem. In this case the vertex detector would not be used for track finding but rather to project back tracks found in the tracking system (TPC) to determine their origin.

An interesting question which has yet to be addressed is whether or not it is possible to tag high energy muons which penetrate the tungsten shielding which in the present design extends to 20° from the beam axis. For example, in the case of $\mu\mu \to \nu\nu W^+W^-$ the primary physics background is due to $\mu\mu \to \mu\mu W^+W^-$. To reduce the background, in addition to a high p_T cut on the WW pair, in might be advantageous to tag forward going muons. These μ's would penetrate the shielding.

9.4.1 Detector Performance Requirements

The detector performance criteria that are used for the design of the detector are summarized in Table 9.5.

The rationale for these particular choices is as follows. A solenoid is the natural field and also has the virtue of curling up soft charged particles. The strength of the field may

need to be increased to trap more particles to a smaller radius. The vertex detector with the tracking will be used for tagging b's from top. The tracking detector requirements are rather modest in terms of momentum resolution, however, there is a large background and so it must have a large number of effective pixels.

The Electromagnetic(EM) calorimeter is used to identify electrons, photons and the core of jets. It is crucial to have high granularity to deal with the background. The low energy photons will interact at the beginning of the EM calorimeter, so longitudinal segmentation will allow it to be reduced in the analysis. The transverse and longitudinal segmentation will also allow the determination of the photon angle to separate photons from the interaction point from background.

The hadron calorimeter must measure jets well enough to separate W's from Z's. Another important measurement will be the missing transverse energy. A study needs to be done to determine the parameters to achieve this goal: energy resolution, e/π response, segmentation, total depth. The parameters listed here are taken from common hadron calorimeters being proposed for current experiments. The segmentation again will help to distinguish the particles from the interaction region from background which will come from upstream.

The muon spectrometer needs to identify and measure muons, but the momentum resolution need not be extraordinary. Again since there will be a large number of muons from sources other than the interaction region, some redundancy will be required to reject the background.

9.4.2 Strawman Detector

The object of this present exercise is to see if a relatively conventional detector can be built using state-of-the-art (or not far beyond) technology to satisfy the physics needs of the muon collider.

A layout of the detector is shown in Fig. 9.39. The main features of the detector are: A large cone (20°) that is probably not instrumented and is used to shield the detector from the machine induced background. The element nearest to the intersection region is the vertex detector located at as small a radius as possible. A number of technologies including Silicon Drift Detectors(SDD), Silicon Pixels [18], and CCD detectors have been considered. Both SDD and pixels will probably work due to their inherent large granularity, but SDD seem especially attractive because of the reduced number of readout channels and potentially easier construction. Inner tracking technologies considered were cathode pad chambers, silicon strips and TPCs. The use of a TPC is interesting as the amount of material is minimized and thus the detector does not suffer as much from low energy photon

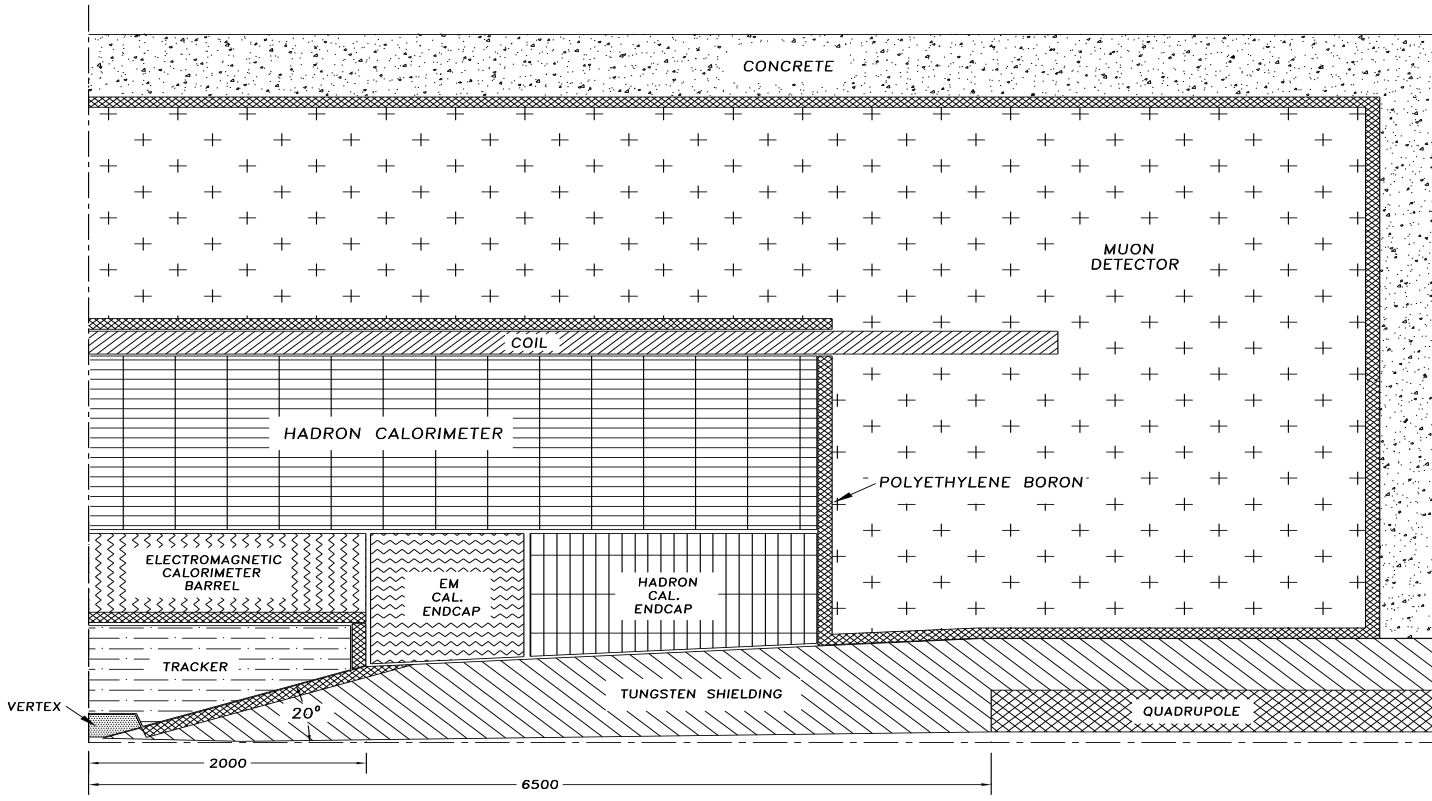

Figure 9.39: Strawman Detector

and neutron backgrounds.

For the calorimeter system there are many options. A liquid argon accordion calorimeter for the EM part [18], [19] and a scintillator hadronic calorimeter appear appropriate. This combination gives a hadronic resolution that is of order $50\%/\sqrt{E}$ which may be good enough. The high granularity of the EM section allows good electron identification which will be of help in tagging b-jets. In addition the longitudinal and transverse granularity allow for corrections on an event by event basis to compensate for the fact that the calorimeter is non-compensating as well as to allow the identification of catastrophic muon bremsstrahlung.

There is a single magnet, with a field of 2 Tesla in the tracking region. The magnet is located behind the hadron calorimeter.

The muon system is a stand-alone system. The chambers in the muon system are Cathode Strip Chambers(CSC) that can be used for both a two dimensional readout as well as a trigger. These chambers have good timing resolution and relatively short drift time which minimizes neutron background problems.

Silicon Drift Vertex Detector

Semiconductor Drift Detectors appear to be an attractive solution for vertexing and inner tracking for an experiment at a $\mu^+\mu^-$ collider. Silicon drift detectors are ideal detector elements for finding secondary vertices and for charged particle tracking close to the interaction region. In the present conceptual design the silicon drift detectors are followed by a large volume Time Projection Chamber (TPC) filled with a fast, low Z gas. The combination of the precise position information provided by the silicon drift detectors and the very good track recognition of the TPC will accomplish all the required tracking tasks, even in the presence of the $\mu^+\mu^-$ collider background.

The $\mu^+\mu^-$ bunches collide once every 10 μs. The background particles produced by the decay of circulating muons and the subsequent cascade processes arrive at the detector at the same time as the particles produced by the studied $\mu^+\mu^-$ interactions. To reconstruct the trajectories of particles produced in the interactions and to reject the background, the highest number of position resolution elements is required. Both tracking technologies use the $10\mu s$ of "clean" time between the bunch crossings to read the position information produced by the particles at the crossing time. One can think of the silicon drift detectors as having an intrinsic signal pipeline within the active volume of the detector. This feature allows a very high detector granularity with a minimum of non-active material in the passage of particles and with a relatively modest number of read–out channels.

Silicon drift detectors are able to provide an unambiguous position resolution of several μm in two perpendicular directions. However, the number of silicon layers is limited and it may be difficult to connect hits in several planes to reconstruct particle tracks in the presence of the low energy photon background. The pattern recognition of the vertex detector will be supplemented by the track information from the TPC.

Silicon drift detectors are able to provide very precise position and ionization measurements with a relatively modest amount of electronics. A perspective view of the drift detector[17] is shown in Fig. 9.40. In principle, the electric field of the drift detector forces electrons liberated by an ionizing particle to drift parallel to the large semiconductor surface to the anode. The transit time of electrons inside the detector measures the distance of an incident particle from the anode. The charge sharing among anodes gives the coordinate perpendicular to the drift direction.

Silicon drift detectors are slowly gaining acceptance in experimental particle physics. CERN experiment NA45 has already published several results obtained with a doublet of cylindrical silicon drift detectors.[20] A similar detector is being used in WA98 and a vertex detector based on a p-type silicon drift detector was approved as an upgrade of experiment

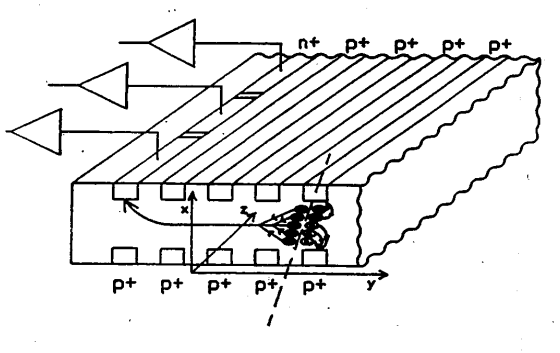

Figure 9.40: Perspective view (not to scale) of a semiconductor drift detector. Electrons created by an ionizing particle are transported long distances parallel to the detector surface. The anode is divided into short segments to measure the coordinate perpendicular to the drift direction.

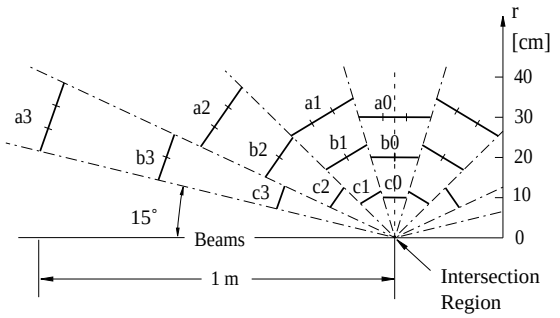

Figure 9.41: Cross section along the beam axis of the vertex and inner tracking detector. Detector has full azimuthal coverage and extends in the polar angle to the shields of the intersection region. Heavy lines indicate the rings of detectors centered around the beam axis.

NA49. At BNL a vertex detector based on silicon drift detectors is being constructed by the STAR collaboration at RHIC.[21]

The best silicon detectors are capable of achieving a position resolution of 4 μm with a detector 300 μm thick. However, these results were obtained only with normally incident charged particles. For other angles of incidence, the resolution can be degraded by the fluctuations in the density of the ionization (Landau) in the silicon. When a fast particle crosses the detector at an inclined angle the detector measures the center of gravity of the charge produced by the particle in a given direction. This center of gravity of the produced charge is on average located in the middle plane of the detector. Due to the fluctuations in the linear density of the ionization, the position of the center of gravity fluctuates in the measured direction. These fluctuations may be larger than the intrinsic resolution of the detector.

The presence of a magnetic field modifies the trajectories of electrons in a silicon drift detector and normal incidence is no longer the ideal one. There is, however, a proper incidence angle which does not give any degradation of the position resolution.

Fig. 9.41 shows the cross section of the proposed silicon drift detector along the beam axis. There is a uniform magnetic field along the beam direction. Different sectors and different layers are visible in Fig. 9.41. Sectors are labelled $0, 1, 2, 3$ and each sector covers a certain region in rapidity. Layers are indicated by letters a, b and c and are placed roughly

30, 20 and 10 cm from the beam. The most important requirement is to maintain a perpendicular incidence of fast particles onto the detector surface to retain the best possible position resolution. There is only a very small overlap between the neighboring sectors. The position of the individual sectors along the beam direction is defined by this non-overlapping requirement, by the desire to maintain normal incidence and by the average distance from the beam axis which is kept constant for all sectors.

The proposed geometry is a possible compromise between the size of the detector in the forward direction and the increase of the density of background particles closer to the intersection point. The geometry minimizes the amount of silicon to cover a given solid angle at any distance. Last but not least the silicon drift detectors in this geometry are less likely to be crossed by low energy spiraling tracks.

The granularity of the proposed detector seems be reasonable for the rates of background particles. Based on rates in Table 9.1 the number of hits, the occupancy and the radiation dose in individual silicon detectors can be estimated. Relevant fluxes are radial for sectors number 0 and longitudinal for sectors number 3. The layer" c0" located 10 cm from the beam has the highest number of hits per cm^2: 11 from the interaction of neutral particles and 16 from crossings of charged particles. For a pixel size of 316×316 μm^2 the number of pixel per cm^2 is 1000. In this case the occupancy of background hits is less than 3% in the layer "c0". Layer c1,c2 and c3 have progressively lower occupancies, the estimated occupancy in the layer c3 being about 2%. The density of background hits decreases almost with the square of the distance from the beams and the occupancies in layers "b" and "a" are less than 1% and 0.4% respectively.

One could even think about locating one more layer, called"d", at about 5 cm from the beams. Detectors with a finer anode pitch than that in the layers farther away would be placed in layer "d". The number of channel would increase only slightly. By also implementing a more sophisticated algorithm for detecting two close hits, the pixel size of the detectors in the "d" layer can be reduced down to 150×150 μm^2. The occupancy of background hits would only be about 3% even in this layer.

The damage due to the radiation dose may be the most annoying problem. If detectors are produced from an n–type silicon with a bulk doping level of $1.5 \times 10^{12}/cm^3$ the detectors have to be replaced after a year of operation. The use of p–type material seems to be more appropriate for this application. P–type silicon drift detectors are being developed in LBNL. These detectors are supposed to be much more radiation resistant. Some R&D may be required.

The decrease of the maximum drift in p–type silicon speed by a factor of 3 is not a problem; the longest drift time can still be shorter than the time between beam crossings.

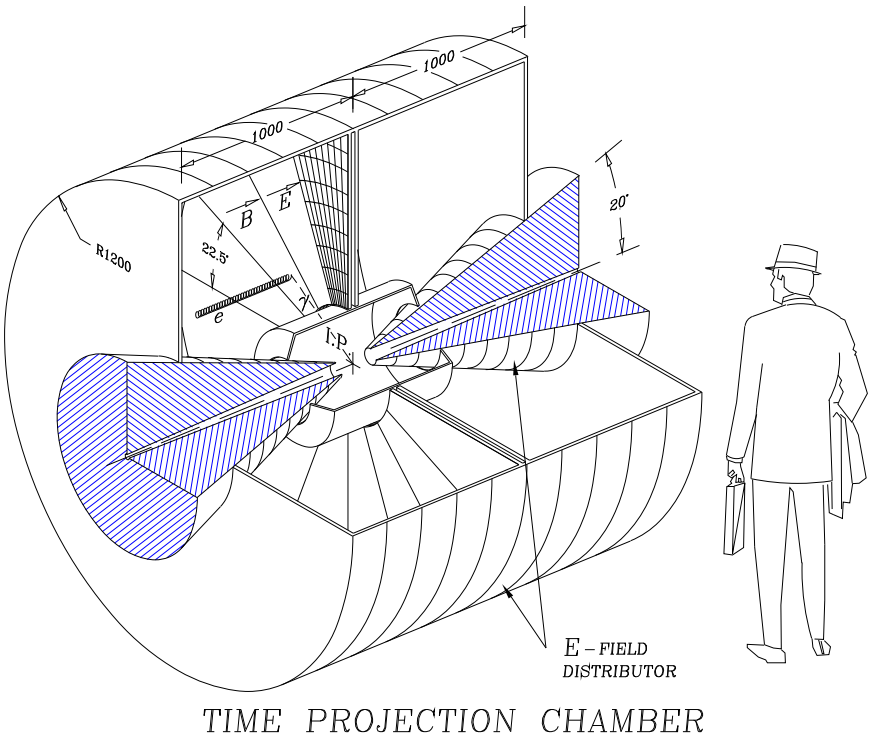

Figure 9.42: Sketch of TPC for Muon Collider Detector.

This is clearly only an initial outline of an inner tracking detector and the real details still remain to be worked out. The number of sectors and number of layers as well as their positions will likely change with a better understanding of backgrounds and with the evolution of the design of the shielding. However it is clear that it should be possible to build such a device for this environment which, at least at 10 cm radius, has a relative low occupancy and which can serve as an excellent vertex detector.

Time Projection Chamber (TPC)

An interesting candidate for tracking at a muon collider is a Time Projection Chamber (TPC). This device has good track reconstruction capabilities in a high density environment, good 3-dimensional imaging and provides excellent momentum resolution and track pointing to the vertex region. It is perhaps particularly well suited to this environment as the long time between bunch crossings ($\sim$ 10 μs) permits drifts of $\sim$1 m and the average density of the device is low compared to more conventional trackers which helps to reduce the measured background rates in the device. In the present detector considerations the TPC would occupy the region between the conic tungsten absorber and electromagnetic calorimeter in the region from 35 cm to 120 cm. (Fig. 9.42)

The TPC is a cylinder, filled with gas at one atmosphere pressure, in parallel axial magnetic and electric fields. The drift region of the TPC is bounded by a field distributor which creates a uniform electric field. The amplification region collects ionization charge and may be a standard cathode pad chamber or any other detector which provides fine readout granularity. The r-ϕ coordinate is measured by interpolating signals on the cathode pads; the r coordinate is given by the pad number and the z coordinate is obtained from the drift time. A special grid is used as a gate to remove undesired events and to significantly reduce the penetration of positive ions into the drift region. The gate is open just before the beam crossing and locked after ~ 2 μs if first level trigger does not appeared.

There are three basic requirements in deciding on a suitable chamber gas for a TPC at a muon collider. To reduce background gamma and neutron interactions in the detector volume, a low density gas mixture should be chosen as the detection medium of the TPC. Another important parameter is the electron drift velocity. Since the time between beam crossings is fixed (10 μs in the present design) the drift velocity should be high enough to collect all the ionization deposited in the drift region. Finally the detection medium should not contain low atomic number gases to help reduce the transfer energy to the recoil nucleus and in this way to reduce its range in the gas. The gas mixture 90% He + 10% CF_4 satisfies all these requirements and it could be an excellent candidate for the TPC. It does not contain hydrogen which would cause a deleterious effect from the neutrons, has a density 1.2 mg/cm^3 and a drift velocity of 9.4 cm/μs. The single electron longitudinal diffusion for this gas is $\sigma_l = 0.15$ mm/$\sqrt{cm}$. The transverse diffusion, which is strongly suppressed by the 2 Tesla magnetic field is given by,

$$\sigma_t = \frac{\sigma_t(B=0)}{\sqrt{1+(\omega\tau)^2}} = 0.03\text{mm}/\sqrt{\text{cm}} \tag{9.1}$$

Each time slice will contain about 25 ionization electrons, and the expected precision in r- ϕ and z coordinates is,

$$\sigma_\phi = \sqrt{\frac{Z\sigma_t^2}{25} + (0.05)^2} \qquad (\text{mm}) \qquad \sigma_Z = \sqrt{\frac{Z\sigma_l^2}{25} + (0.15)^2} \qquad (\text{mm}) \tag{9.2}$$

Z - drift length (cm). The precision of r-coordinate is defined by the anode wire pitch - 3mm.

Low energy photons, neutrons and charged particles produce the main background for the inner tracker. Photons in the MeV region interact with matter mainly by Compton scattering. For a 1 MeV photon the probability of producing a Compton electron in 1 cm of gas is $\xi_\gamma = 4.5 \cdot 10^{-5}$. For an average photon fluence $h_\gamma = 100$ cm^{-2} about $N_\gamma = 4 \cdot 10^4$ electron tracks are created in the chamber volume. Because the transverse momentum of Compton electrons is rather small the electrons are strongly curled by the magnetic field

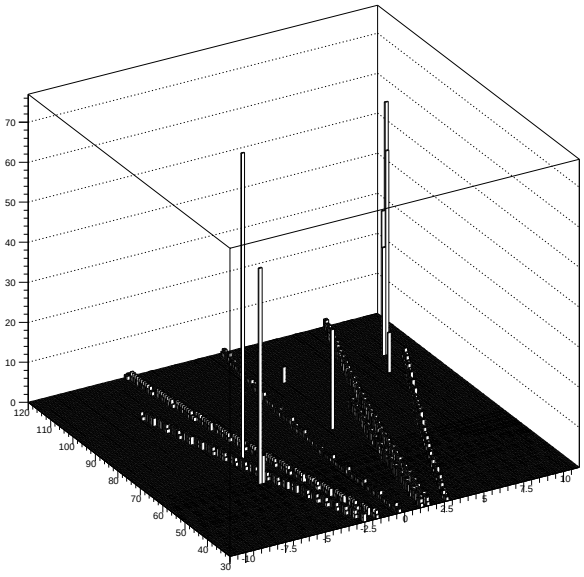

Figure 9.43: Number of digitized points in an xy cell from a signal event and background Compton electrons.

and move along the magnetic field lines. Most of the electrons have a radius less than one millimeter and their projection on the readout plane covers not more than one readout pitch, 0.3×0.4 cm^2. The average length of the Compton electron tracks in the TPC is one meter and therefore, the volume occupied by electron tracks is $v_{comp.e} = 4.8 \cdot 10^5$ cm^3. Since the total chamber volume is 10^7 cm^3, the average occupancy due to background photon interactions is equal to,

$$< occupancy >_\gamma = \frac{V_{comp.e}}{V_{total}} = 4.4 \cdot 10^{-2} \tag{9.3}$$

For neutrons in the MeV region the primary interaction with matter is elastic collisions. In this case the energy transfer to the nucleus has a flat distribution and the maximum transfer energy is given by $4E_nA/(A+1)^2$ or $4E_n/A$ when $A \gg 1$. The maximum transfer momentum is $P_{max} = \sqrt{2m_pE_n}$ for H and $P_{max} = \sqrt{8m_pE_n}$ for $A \gg 1$. The ionization energy loss for slow heavy particles is,

$$dE/dx \propto (Z/\beta)^2 = (ZE_{total}/P)^2 \tag{9.4}$$

Z - nucleus charge, E_{total} - total nucleus energy, P - nucleus momentum. Taking into account that $E_{total} \approx A \cdot m_p$,

$$dE/dx \propto \frac{1}{2} \cdot \frac{m_p}{E_n} \qquad (forH) \qquad dE/dx \propto \frac{A^4}{32} \cdot \frac{m_p}{E_n} \qquad (forA \gg 1) \tag{9.5}$$

The calculated mean energy of background neutrons is $E_n = 27\ MeV$. In this case, for hydrogen, the ionization loss of recoil protons is about 20 times higher than for minimum

ionizing particles, that is $dE/dx \approx 20\ keV/cm$ and their mean range in the gas is several meters. For carbon, for example, the ionization loss is much higher and $dE/dx \approx 24\ MeV/cm$. This implies that for the gas chosen, the mean length of the recoil nucleus tracks will only be a few millimeters. This simple estimation shows that the operating gas of the TPC should not contain hydrogen to exclude long range tracks in the chamber volume.

The occupancy due to background neutron interactions can be estimated as follows. The calculated neutron fluence is $< n >= 10^3\ cm^{-2}$. As discussed above the track of the recoil nucleus occupies, typically, not more than one volume cell of the TPC, $v_n = 0.3{\times}0.4{\times}1.0$ cm^3. The probability of a background neutron interacting in 1 cm of the gas is $\xi_n = 2 \cdot 10^{-5}$, the number of recoil tracks $N_n =< n > \cdot \xi_n \cdot V_{total} = 2 \cdot 10^5$ and therefore the neutron occupancy is,

$$< occupancy >_n = \frac{N_n \cdot v_n}{V_{total}} = 0.24 \cdot 10^{-2} \tag{9.6}$$

The overall background occupancy is not very high. However, given the number of background tracks, it may be difficult to extract the event tracks without any cleaning procedure. To optimize chamber performance and to study the efficiency of 'cleaning' algorithms a chamber simulation program was developed. This simulation of high momentum event tracks and background tracks includes ionization, drift and diffusion electrons in the gas, multiplication and other details of the detection process. The volume of the TPC was divided into 1 cm z slices and each piece of track crossing such a slice was digitized for each pad row on which it induces charge. In this way each piece of track transfers to a three dimensional point.

It is easy to clean out the recoil tracks owing to their large ionization density per cell. To do this only a simple cut to remove all volume cells which contain a charge in excess of some preset threshold is required. This cut will only eliminate about 1% of the TPC volume.

The Compton tracks can be removed in a similar way. Again the volume of the TPC is divided into 1 cm z slices and each piece of track crossing such a slice was digitized for each pad row on which it induces charge. The result is that each piece of track transfers to a three dimensional point. Then all the digitized points from the TPC volume are projected on the readout plane which is divided into 0.3×0.3 cm^3 cells. After that, the number of points contained in each cell is computed. Because almost all points of a Compton track lie along the z-axis most of them will be projected into one cell and therefore the number of points in this cell will be very different from hit cells from non-background tracks. Fig. 9.43 clearly demonstrates the difference between the high momentum event tracks and the low energy Compton electron tracks. It is obvious that to remove low momentum electron tracks, all cells containing more than some threshold number of points should be excluded. Applying this procedure a few percent of volume is lost but the quality of the high momentum tracks

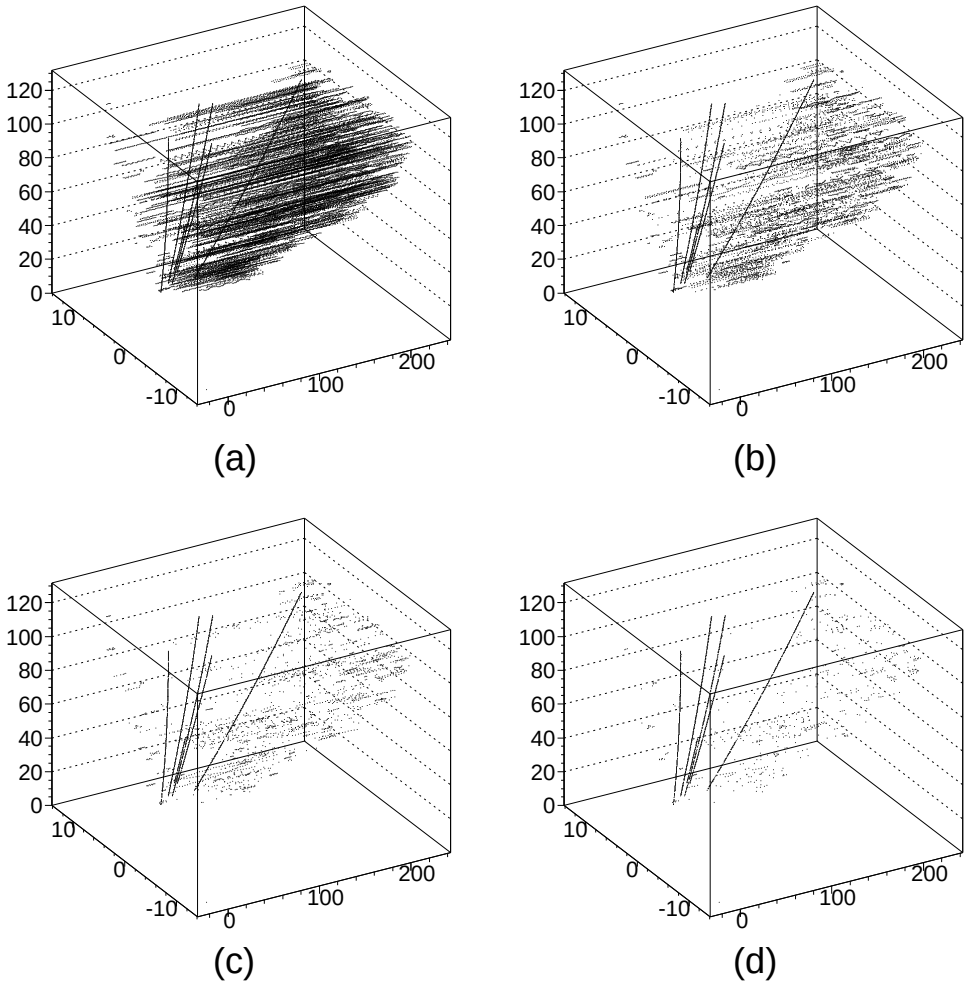

Figure 9.44: Charge distribution from a signal event and background Compton electrons with threshold cuts; (a) has no cut applied while (d) has the most stringent cut.

is not substantially changed. This is clearly illustrated in Fig. 9.44 where one sector of the TPC is shown after the application of different value threshold cuts.

Once the clean up from neutron and Compton background is carried out, some information about TPC performance can be obtained. Fig. 9.45a shows the transverse momentum resolution for tracks with $P_t = 50\ GeV/c$. The momentum resolution is about 1.2% in this case. In Fig. 9.45b the difference along the x-axis between the real vertex and the vertex interpolated from track intersections is shown. For these distributions tracks were generated uniformly in η and $P_t \geq 10\ GeV/c$. In neither case has information on the bunch crossing point been used.

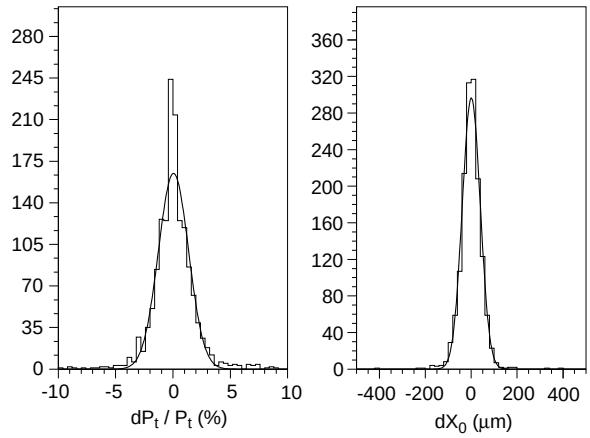

Figure 9.45: Momentum (a) and position (b) resolution for the TPC.

Electromagnetic Calorimeter

An accordion liquid argon calorimeter is being developed for the ATLAS collaboration[18]. A similar calorimeter designed for the GEM Collaboration at the SSC is shown in Fig. 9.46[19].

The calorimeter is made of a sandwich of stainless steel clad lead absorber plates interleaved with Kapton electrodes. Both are bent into a corrugated shape - hence the name accordion. The plates are arranged roughly radially for the barrel calorimeter so that there are no through going cracks. The Kapton electrodes can be subdivided to measure θ and depth according to the requirements of the experiment. The electrodes are ganged together in ϕ again according to the design. In this way, almost arbitrary segmentation can be achieved in all three directions: θ, ϕ and depth. Liquid argon calorimeters have shown high radiation resistance and excellent timing resolution[22]. In ATLAS a design for the end cap geometry called the "Spanish Fan" has also been successfully tested.

The large amount of hadronic energy deposited in the calorimeter is mostly in the form of low energy particles. Most of this energy will be deposited in the first section of the EM calorimeter and to handle it will require both transverse and longitudinal segmentation in the calorimeter. This will allow one to reconstruct the energy of the particle coming from the intersection region by using the added information on its direction as well as longitudinal shower development.

From the GEANT background calculations, the total energy deposited from the electromagnetic debris is $\sim$ 13 TeV. However, if one divides the calorimeter into $\sim 2\times10^5$ cells, the mean energy would be about 65 MeV/cell. Certainly, energetic electromagnetic showers from γ's or electrons or the core of jets will stand out above this uniform noise. Since the readout is every 10 μs, multiplexing is possible to reduce costs compared to the LHC where collisions occur every 25 ns.

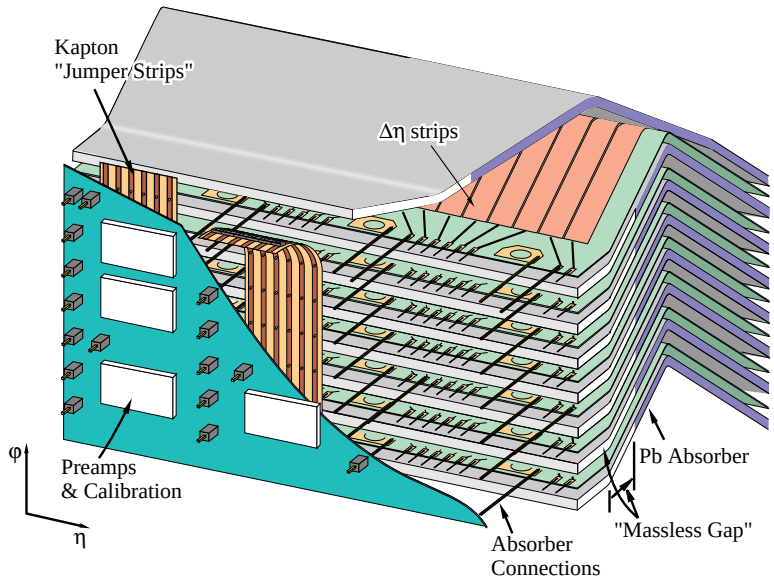

Figure 9.46: Liquid argon accordion calorimeter designed for the GEM experiment. The strips measure the azimuthal angle.

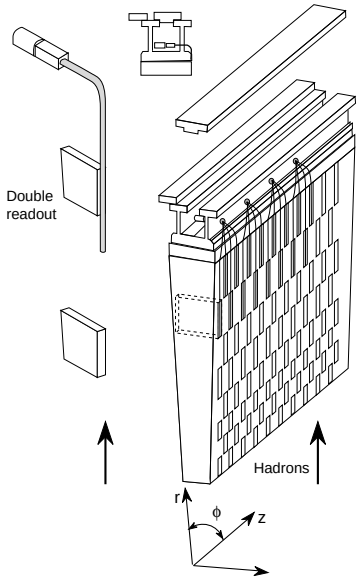

Figure 9.47: Scintillator tile calorimeter from the ATLAS experiment.

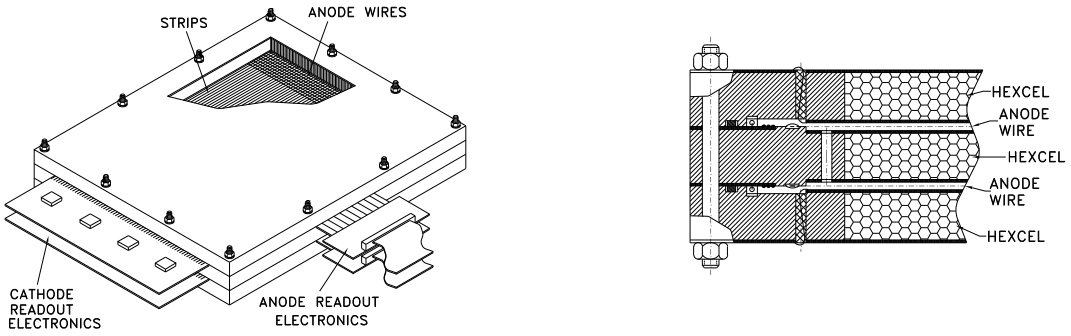

Figure 9.48: A two-layer module of the Cathode Strip Chamber.

Hadron Calorimeter

A good choice for the hadron calorimeter is a scintillator tile device being designed for ATLAS[18]. It uses a novel approach where the tiles are arranged perpendicular to the beam direction to allow easy coupling to wave-length shifting fibers[23]Fig. 9.47

From the GEANT background calculations, the total energy deposited in the calorimeter from electromagnetic and hadronic showers and muons is about 100 TeV. Again, this is rather uniform with a low mean energy per cell. It should be thought of as a sort of pedestal noise and should not affect the measurement of jets. With a tile calorimeter of the type discussed here it should be possible to achieve a resolution of Δ E/E$\sim$ 50%/$\sqrt{\mathrm{E}}$

Muon Spectrometer

Triggering is probably the most difficult aspect of muon spectrometers in large, 4π detectors in both lepton and hadron colliders. In addition, a muon system should be able to cope with the larger than usual muon backgrounds that would be encountered in a muon collider. Segmentation is, again, the key to handling these high background rates. Cathode Strip Chambers (CSC) are an example of a detector that could be used in the muon system of a muon collider experiment. CSCs are multi-wire proportional chambers (MWPC) with segmented cathodes so they provide measurements of both coordinates. The coordinate along the anode wires can be determined with high precision (of order 50 μm) by determining the center of gravity of the charge induced on the cathodes by the electron avalanche. The resolution in the transverse coordinate is limited by the anode wire spacing (just as in traditional MWPCs) and is of the order of one mm. Coarser strips can be used if such resolution is not needed. The short maximum drift time (of order 35 ns) allows bunch crossing identification as well as prompt signals that can be used for triggering. Thus one

detector performs all functions necessary for a muon system:

- Precision coordinate(50 to 70 μm)
- Transverse coordinate(of order mm or coarser as needed)
- Timing (to a few ns)
- Trigger primitives

In addition, the cathodes can be lithographically segmented almost arbitrarily resulting in pixel detectors the size of which is limited only by the density and signal routing of the readout electronics.

Cathode strip chambers were first developed as pixel (or pad) chambers for an experiment at the AGS (E814) to handle the high secondary particle densities in heavy ion collisions. They were further developed for muon identification and measurement for the GEM experiment at the SSC[25]. They have been adopted for use in parts of the muon systems of both CMS and ATLAS experiments at the LHC as well as the muon arms of the PHENIX experiment at RHIC. An effort to develop a monolithic front end is well under way at BNL with fully functional prototypes already fabricated and tested.

A detector is usually built as a multi-layer module. The CSC design, shown in Fig. 9.48 has two layers formed by three flat, rigid panels, each made of a 23 mm thick sheet of nomex honeycomb (hexcel) and two 1.19 mm thick copper-clad FR4 laminates (Fig. 9.48b), the 17 μm thick copper forming the cathodes. The panel frames are made of machined zelux (fiberglass reinforced lexan). They provide the 2.54 mm step for the anode plane of gold-plated tungsten wires 30 μm in diameter. The frames of the outer panels have a milled cavity with enough room for epoxy beads for the wire attachment as well as the anode blocking capacitors. A rubber gasket just outside this cavity provides the gas seal for the assembly. In this manner no components under high voltage are outside the seal, thus minimizing the risk of high voltage breakdowns.

The position sensing cathode strips are lithographically etched on either side of the central panel. These cathodes are precisely positioned with respect to each other with the aid of locating pins. The strips are oriented at 90° with respect to the anode wires, providing precision position measurement in the direction along the anode wires. The outer cathodes in each layer are segmented in orthogonal strips or left as continuous (un-etched) copper planes if the wires are read out to provide the transverse coordinate. The cathode readout pitch, W, is 5.08 mm. With a 1% charge interpolation this readout spacing provides a resolution of $\approx 50\mu m$. The interpolation precision is limited by the signal to noise ratio and,

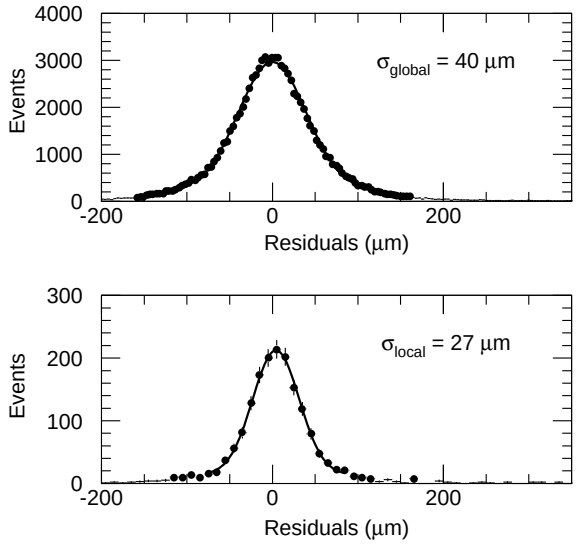

Figure 9.49: Typical spatial resolution of the Cathode Strip Chamber.

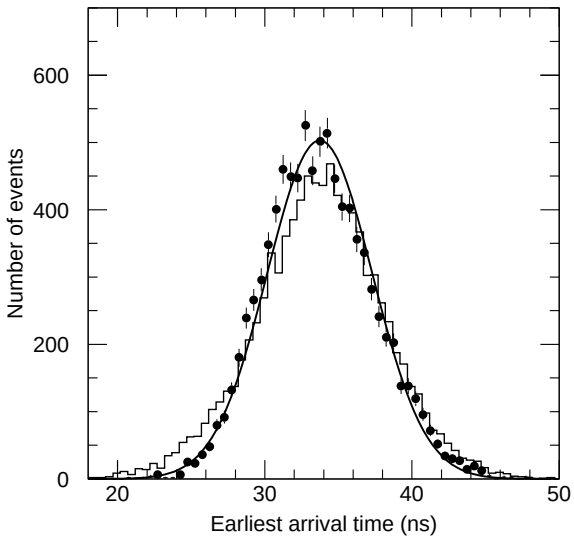

Figure 9.50: Typical timing resolution of the Cathode Strip Chamber.

in principle, can be improved for a given electronic noise by increasing the gain. In practice inter-calibration of neighboring channels and geometric deviations eventually set the limit in the achievable resolution. Prototype CSC detectors have been constructed for both the GEM and ATLAS experiments. Fig. 9.49 shows the measured resolution from such a prototype.

Although the maximum drift time for typical gases is of order 35 ns, event timing with an rms of a few ns can be achieved in a multilayer module by determining the earliest time of arrival from all layers. Fig. 9.50 shows the measured timing resolution in the same prototype.

9.5 Backgrounds for a 250 GeV x 250 GeV Collider.

Work has begun on estimating the various machine related backgrounds for a 250 GeV x 250 GeV muon collider. Since no real final focus or lattice design for such a machine exists at this time the dimensions for the lower energy machine are just scaled from the higher energy machine: the longitudinal dimensions were divided by the square root of 8 while the radial dimensions and the fields were identical to the 4 Tev case. It is also assumed that the machine will have 8 Tesla dipoles resulting in a ring 650 meters in circumference, that there will be only one bunch per fill and consequently a bunch crossing every 2 microseconds. The initial luminosity will be reduced by 50 percent after 1000 loops, and an initial bunch of 10^{12} muons will generate 1.5×10^6 decay electrons every meter. The final focus extends 46 meters from the intersection point and contains only quadrupoles. The last quadrupole ends

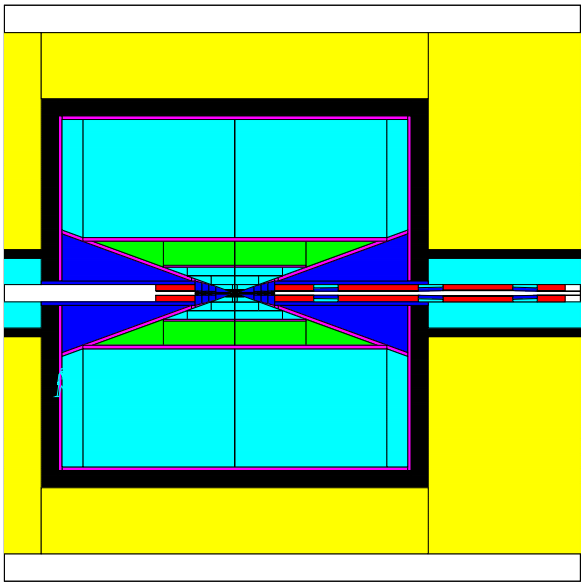

Figure 9.51: Intersection region for 250 GeV x 250 GeV Machine.

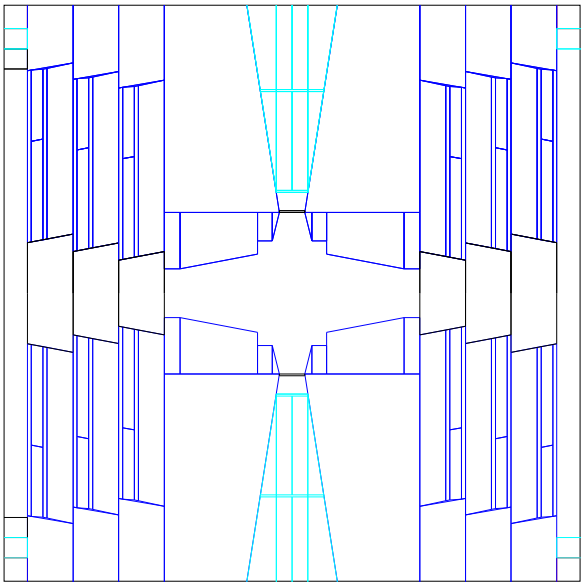

Figure 9.52: GEANT description of Intersection region for 250 GeV x 250 GeV machine.

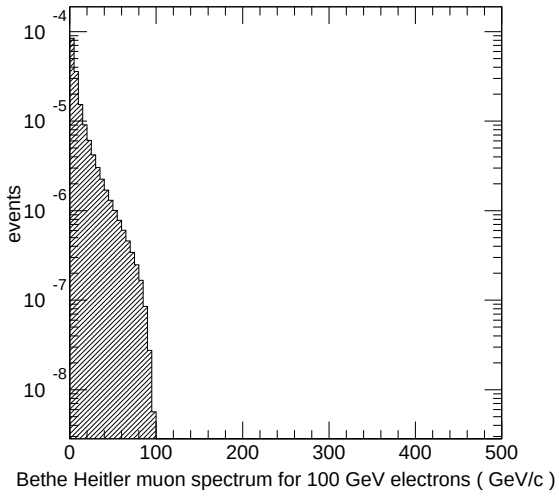

Figure 9.53: Bethe–Heitler muon spectrum from a 100 GeV electron.

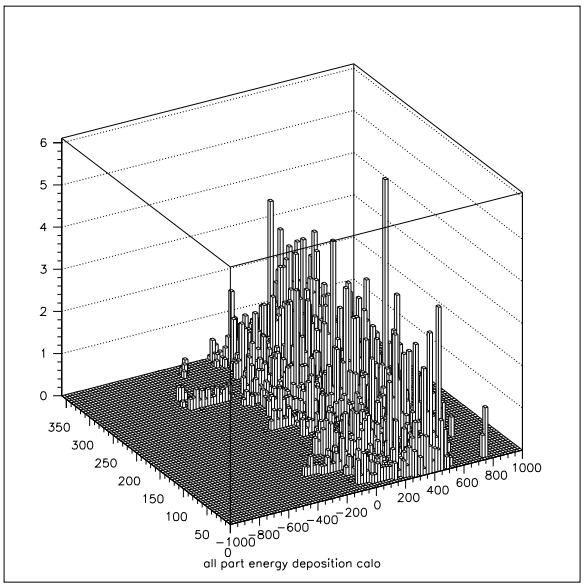

Figure 9.54: Energy deposited by muons in the calorimeter.

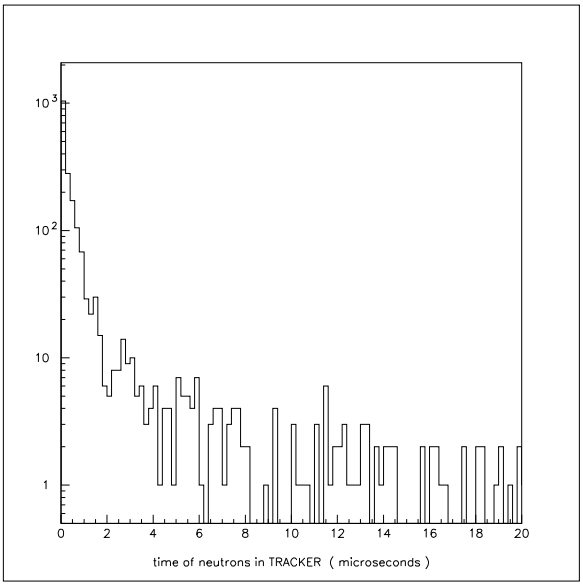

Figure 9.55: Neutron time of flight.

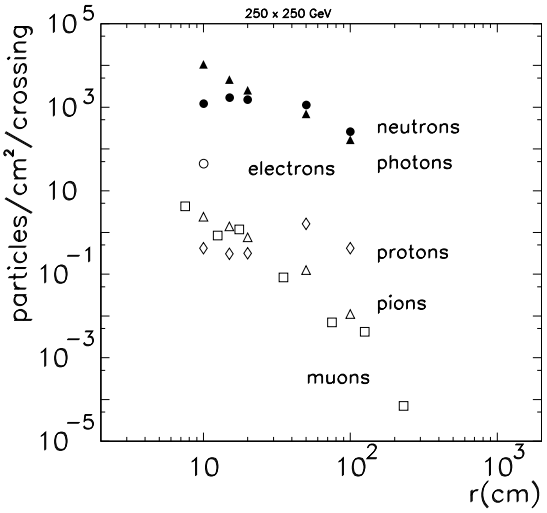

Figure 9.56: Fluences for the 250 GeV X 250 GeV machine.

2.3 meters from the IP and as in the 4 Tev case all the backgrounds generated outside the final focus region are ignored.

The average energy of the electrons from muon decay is 88 GeV. The critical energy of the synchrotron radiation has an average of 21.4 MeV, resulting in an average photon energy of 16.5 MeV. The fraction of electron energy carried by synchrotron radiation photons is only 1.65% compared to 20% for the 4 Tev case.

The same methods used for the 4 Tev study were applied in the present study. The experimental area is again a cylindrical cavity of 10 meter radius and 20 meters length Fig. 9.51. The final focus geometry here is much more compact and there are no toroids between the final focus quadrupoles. The σ_x and σ_y envelope of the muon bunch in the spaces between the quadrupoles was calculated and non-magnetic scrapers with ellipsoidal apertures of 4σ were assumed in transporting the decay electrons. The beam aperture at the exit of the last quad is 2.5 cm and the shielding material used is tungsten. The same inverted cones method for the shield design was used. In this case the angle is 11 mrad compared to 4 mrad for the 4 Tev machine. The final shield around the IP starts at 1.1 m and has an opening of 1.2 cm radius compared to 0.42 cm for the 4 Tev machine. This leaves the intersection region more exposed to electromagnetic debris than was the case for the 4 Tev machine. The details of the 250 GeV design can be seen in Fig. 9.52.

The spectrum of Bethe–Heitler muons for a 100 GeV electron hitting the tungsten shielding is shown in Fig. 9.53. The probability for Bethe–Heitler muon production, as a function

of electron momentum is shown in Fig. 9.21. The average momentum of the Bethe–Heitler muons generated in the whole final focus region is 10.1 GeV and they have an average relative angle to the electron direction of 18 mrad. The average probability of a decay electron to produce a Bethe–Heitler muon is 1.2×10^{-4}.

The total energy deposited in the calorimeter (333 Tev) has three main contributions : 35 Tev is pure electromagnetic, 297 Tev is from hadronic sources and 1.2 Tev is deposited by the Bethe–Heitler muons. The energy deposited by muons is shown in Fig. 9.54.

Another difference from the 4 Tev collider is the fact that the bunch crossings here occur every 2 microseconds. Since there is a high flux of slow neutrons, the neutrons surviving from the previous crossings were estimated. In Fig. 9.55 the timing of neutrons relative to the bunch crossing is shown. It is evident that for a 2 microsecond gate, the contribution from previous crossings is only at the 1% level.

The fluences for different particles are shown in Fig. 9.56. They are all radial fluxes except for the muons where a longitudinal flux is preferred. All the backgrounds are comparable to those for the 4 Tev collider. In other words, the lowering of the energy by a factor of 8 compensates for the order of magnitude increase in the rate of muon decay.

This is only a very preliminary analysis of the machine related backgrounds for the 250 GeV x 250 GeV collider. The positions and strengths of the magnets were not optimized. From the point of view of background reduction, one would prefer a much bigger distance between the end of the last quadrupole and the IP. This would make the hadronic shield deeper and will reduce the 1.2 cm radius of the iris which controls the photon flux .

9.6 Summary and Conclusions.

Two independent background calculations have been used for a preliminary study of the expected background level at a 4 TeV muon collider. The optimization of the intersection region is still at its infancy, but the results of both studies show that the level of background while still large, can be managed with proper design of the intersection region and choice of detector technologies. This is in large part due to the fact that the background is composed of many very soft particles which behave like a pedestal shift in the calorimeter. The tracking and vertexing systems will have to be highly segmented to handle this flux of background particles.

A large amount of work is still needed in order to optimize the intersection region and the final focus. In particular a better understanding of the trade off between the different backgrounds is required.

The strawman detector presented here is meant only to show that the muon collider

detector has unique problems and advantages. An optimized detector needs to be developed taking these problems into consideration. Present state-of-the-art technologies seem to be sufficient to build a detector which will meet the physics requirements of a 4 TeV collider. There is still a large amount of uncertainty and more studies are needed. In particular, the vertex detector and calorimeter performance in this level of background needs to be studied.

Some preliminary calculations for machine related backgrounds for a lower energy collider (250 GeV x 250 GeV) have also been carried out. It appears at this time that the backgrounds in this case are comparable to the levels at the 4 Tev machine. Since little attention has yet been paid to the details of the final focus for this lower energy machine it is possible that reductions in the machine related backgrounds will be achievable in the future.

Bibliography

[1] For references to in-depth studies of physics at future e^+e^- colliders, see e.g. *Proceedings of the Workshop on Physics and Experiments with Linear Colliders*, ed. F.A.Harris, *et al.*, World Scientific(1993); *Proceedings of the Workshop on Physics and Experiments with Linear e^+e^- Colliders*, Wailkoloa, Hawaii(April 1993), ed. F. Harris *et al.*,(World Scientific, 1993); JLC Group, KEK Report 92-16(1992); *Proceedings of the Workshop on Physics with Linear Colliders*, Saariselkä, Finland(Sept. 1991), ed. R. Orava *et al.*, World Scientific (1992).

[2] See e.g. *Proceedings of the First Workshop on the Physics Potential and Development of $\mu^+\mu^-$ Colliders*, Napa, California, 1992, Nucl. Instr. and Meth. **A350**, 24(1994).

[3] 13) THE MAD PROGRAM. By H. Grote, F.C. Iselin, E. Keil (CERN), J. Niederer (Brookhaven). CERN-LEP-TH-89-13, Mar 1989. 4pp. Presented at 1989 Particle Accelerator Conf., Chicago, IL, Mar 20-23, 1989. Published in IEEE Part.Accel.1989:1292-1294.

[4] V. Barger, *et al.*, Phys.Rev. **D52**, 3815(1995).

[5] I. J. Ginzburg, *The e^+e^- pair production at $\mu^+\mu^-$ collider*, Preprint: hep-ph/9601273(1996).

[6] P. Chen, *Beam-Beam Interaction in Muon Colliders*, SLAC-PUB-7161(April, 1996).

[7] R. L. Ford and W. R. Nelson, *The EGS Code System: Computer Programs for the Monte Carlo Simulation of Electromagnetic Cascade Showers*, SLAC-0210, Jun 1978.

[8] A. Fasso, A. Ferrari, J. Ranft and P. R. Sala, *FLUKA: present status and future developments*, Proc. of the IV Int. Conf. on Calorimetry in High Energy Physics, La Biodola (Is. d'Elba), Italy(Sept. 20-25 1993), Ed. A. Menzione and A. Scribano, World Scientific, p. 493(1993).

[9] C. Zeitnitz and T. Gabriel, Nucl. Instr. Meth., **A349**, p. 106 (1994).

[10] N. V. Mokhov, *The* MARS *Code System User's Guide, version 13 (95)*, FNAL–FN–628 (1995).

[11] N. V. Mokhov, *Comparison of Backgrounds in Detectors for LHC, NLC and $\mu^+\mu^-$ Colliders*, in Proceedins of the Symposium on Physics Potential and Development of $\mu^+\mu^-$ Colliders, San Francisco, CA, December 1995; Fermilab–Conf–96/062.

[12] A. I. Drozhdin, M. Huhtinen and N. V. Mokhov, *Accelerator Related Background in the CMS Detector at LHC*, Fermilab–Pub–96/113 and CERN CMS TN/96-056 (1996).

[13] G. W. Foster and N. V. Mokhov, *Backgrounds and Detector Performance at a 2+2 TeV $\mu^+\mu^-$ Collider*, in *AIP Conference Proceedings*, **352**, pp. 178-190 (1995); also Fermilab–Conf–95/037 (1995).

[14] N. V. Mokhov and S. I. Striganov, *Simulation of Backgrounds in Detectors and Energy Deposition in Superconducting Magnets at $\mu^+\mu^-$ Colliders*, Proceedings of the 9th Advanced ICFA Beam Dynamics Workshop, Ed. J. C. Gallardo, AIP Conference Proceedings 372, 1996.

[15] Yung-Su Tsai, Review of Modern Phys., **46**, 4(1974).

[16] *The Time Projection Chamber: A New 4π Detector for Charged Particles*, D.R. Nygren (SLAC). PEP-0144, (Received Dec 1976). 21pp. In Berkeley 1974, Proceedings, Pep Summer Study, Berkeley 1975, 58-78.

[17] E. Gatti and P. Rehak, Nucl. Instr. and Meth. **225**, 608 (1984).

[18] *ATLAS Technical Proposal for a General-Purpose pp Experiment at the Large Hadron Collider at CERN*, CERN/LHCC/94-43, LHCC/P2 (15 December 1994).

[19] *GEM Technical Design Report Submitted by Gammas, Electrons, and Muons Collaboration to the Superconducting Super Collider Laboratory*, GEM-TN-93-262; SSCL-SR-1219 (July 31, 1993).

[20] G. Agakichev, *et al.*, Phys. Rev. Lett., **75**, 1272(1995).

[21] *The STAR Experiment at the Relativistic Heavy Ion Collider*, Nucl. Phys., **A566**,1994.

[22] O. Benary, *et al.*, Nucl. Inst. and Meth., **A332**, 78(1993).

[23] O. Guidemeister, F. Nessi-Tadaldi and M. Nessi, Proc. 2nd Int. Conf. on Calorimetry in HEP, Capri, 1991.

[24] P. Rehak and E. Gatti, *Intersection between Particle and Nuclear Physics*, AIP Conference proceedings 338, 320 (1995).

[25] G. Bencze *et al.*, Nucl. Inst. and Meth., **A357**, 40(1995).

Contributors

- D. Lissauer, (BNL) Editor
- A. Baltz, (BNL)
- O. Benary, (Tel-Aviv Univ.)
- S. Geer, (FermiLab)
- H. Gordon, (BNL)
- S. Kahn, (BNL)
- P. Lebrun, (FermiLab)
- A. Luccio, (BNL)
- H. Ma, (BNL)
- N. Mokhov, (FermiLab)
- M. Murtagh, (BNL)
- F. Paige, (BNL)
- R. B. Palmer, (BNL)
- V. Polychronakos, (BNL)
- S. Protopopescu, (BNL)
- P. Rehak, (BNL)
- I. Stumer, (BNL)
- H. Takai, (BNL)
- V. Tchernatine, (BNL)
- A. Tollestrup, (FermiLab)
- W. Willis, (Columbia Univ.)

List of Figures

List of Tables